CHEMISTRY

Stabilizing Co_2C with H_2O and K promoter for CO_2 hydrogenation to C_{2+} hydrocarbons

Mingrui Wang[1], Peng Wang[2], Guanghui Zhang[1]*, Zening Cheng[3], Mengmeng Zhang[1], Yulong Liu[1], Rongtan Li[4], Jie Zhu[1], Jianyang Wang[4], Kai Bian[1], Yi Liu[1], Fanshu Ding[1], Thomas P. Senftle[2]*, Xiaowa Nie[1], Qiang Fu[4], Chunshan Song[5]*, Xinwen Guo[1]*

The decomposition of cobalt carbide (Co_2C) to metallic cobalt in CO_2 hydrogenation results in a notable drop in the selectivity of valued C_{2+} products, and the stabilization of Co_2C remains a grand challenge. Here, we report an in situ synthesized K-Co_2C catalyst, and the selectivity of C_{2+} hydrocarbons in CO_2 hydrogenation achieves 67.3% at 300°C, 3.0 MPa. Experimental and theoretical results elucidate that CoO transforms to Co_2C in the reaction, while the stabilization of Co_2C is dependent on the reaction atmosphere and the K promoter. During the carburization, the K promoter and H_2O jointly assist in the formation of surface C^* species via the carboxylate intermediate, while the adsorption of C^* on CoO is enhanced by the K promoter. The lifetime of the K-Co_2C is further prolonged from 35 hours to over 200 hours by co-feeding H_2O. This work provides a fundamental understanding toward the role of H_2O in Co_2C chemistry, as well as the potential of extending its application in other reactions.

INTRODUCTION

The continuously increasing greenhouse gas CO_2 levels originated from human activities have caused a series of environmental issues, including sea level rises, heat waves, and ocean acidification (1). Among the strategies considered, catalytic CO_2 reduction with green H_2, which is generated from water splitting by renewable energy, to valuable C_{2+} hydrocarbons (HCs) provides a potential technology to reduce CO_2 concentration and an alternative nonpetroleum-based production route toward light olefins ($C_2 \sim C_4^=$) and liquid fuels (C_{5+}) (2, 3). However, the chemical inertness of CO_2 molecules (C=O bond of 750 kJ mol^{-1}) and the high energy barrier of C—C coupling are detrimental to the formation of C_{2+} products (4, 5). Accordingly, it is highly attractive and challenging to develop effective catalysts for selective CO_2 conversion to C_{2+} HCs.

Much attention has been paid to using CO Fischer-Tropsch synthesis (CO-FTS) catalysts for CO_2 hydrogenation, and, in general, CO_2 is initially converted to CO intermediate via a reverse water gas shift (RWGS) reaction, followed by CO hydrogenation to C_{2+} HCs (6). For instance, iron carbide (FeC_x) exhibits high activity for CO_x hydrogenation to olefins in a high-temperature range (320° to 350°C) (7–9). Cobalt carbide (Co_2C) is also a promising catalyst for CO_x conversion owing to its adequate activation of C=O bonds and promoting effect on C—C coupling (10). Notably, it has distinct features in different reaction atmospheres. As for CO-FTS, nanoprism Co_2C with preferentially exposed

(101) and (020) facets has been proven to be responsible for the synthesis of $C_2 \sim C_4^=$, while electronic (alkali metal) and structural promoters (Mn and Ce) are instrumental in its morphological control (11–15). The synthesis of Co_2C is commonly divided into two steps, including an initial reduction and carburization in syngas (CO and H_2) or CO. Wavelet transform and linear combination fitting results of in situ x-ray absorption spectroscopy (XAS) indicate that cobalt oxide (CoO) is first reduced to metallic cobalt (Co^0), and then carburized to Co_2C (16). Moreover, Co_2C is commonly used below 260°C and at near atmospheric pressure in CO-FTS to avoid its decomposition to Co^0 and graphite (17). Despite numerous efforts, Co_2C is unstable and still underutilized for CO_2 hydrogenation (18, 19). Compared with CO-FTS, the conversion of equimolar CO_2 consumes more H_2, and the presence of excess H_2 and CO_2 accelerates the decomposition of presynthesized Co_2C (18). Besides, the activation of inert CO_2 often requires a high temperature, and it thus puts forward higher requirements for the thermal stability of Co_2C. As a result, the Co_2C catalyst tends to partially decompose to Co^0 under CO_2 hydrogenation, which leads to a rapid side reaction toward CH_4 (20). In recent studies, SiO_2 support interacted with Co_2C was used for improving the stability, but a reconstruction to Co^0 occurred while C_1 products dominate under reaction conditions (21). Co_2C with different morphologies was prepared from the ZIF-67 precursor by Zhang et al. (22) for RWGS reaction, but the atmospheric pressure condition only enables a reduction of CO_2 to CO and limits the selectivity to C_{2+} HCs. The facile synthesis and stabilization of Co_2C under a C-lean and H-rich atmosphere at higher temperatures and pressure are major bottleneck for its catalytic application in CO_2 hydrogenation to C_{2+} HCs.

H_2O is a common impurity for CO_2 capture from flue gas (23), and more H_2O is generated in CO_2-FTS compared with CO-FTS; therefore, its impact on the catalyst structure and performance needs to be pinpointed. As for Fe-based catalysts, H_2O-induced oxidation causes the evolution of FeC_x to iron oxides (FeO_x) and a decrease of the activity in both CO- and CO_2-FTS (8, 24). H_2O has also

[1]State Key Laboratory of Fine Chemicals, Frontier Science Center for Smart Materials, PSU-DUT Joint Center for Energy Research, School of Chemical Engineering, Dalian University of Technology, Dalian 116024, China. [2]Department of Chemical and Biomolecular Engineering, Rice University, Houston, TX 77005, USA. [3]Zhundong Energy Research Institute, Xinjiang Tianchi Energy Co., Ltd., Changji 831100, China. [4]State Key Laboratory of Catalysis, Dalian National Laboratory for Clean Energy, Dalian Institute of Chemical Physics, Chinese Academy of Sciences, Dalian 116023, China. [5]Department of Chemistry, Faculty of Science, The Chinese University of Hong Kong, Shatin, NT, Hong Kong SAR, China.
*Corresponding author. Email: gzhang@dlut.edu.cn (G.Z.); tsenftle@rice.edu (T.P.S.); chunshansong@cuhk.edu.hk (C.S.); guoxw@dlut.edu.cn (X.G.)

been proven as a poison owing to its competitive adsorption and oxidation of Co^0 catalyst in CO-FTS (25–27). Thus, the rapid removal of H_2O boosts the syngas conversion to C_{2+} HCs (28). However, up to now, the effect of H_2O on Co_2C catalyst is still ambiguous in CO_2 hydrogenation, clarification, and optimization which is of importance to improving the practical application.

Here, we report the in situ synthesis and stabilization of Co_2C with H_2O from a K-modified Co_3O_4 precursor for CO_2 hydrogenation. In situ x-ray diffraction (XRD) and simulated results of chemical potential corroborate that the carburization route derived from CoO dominates under CO_2 hydrogenation conditions, while the reaction atmosphere in conjunction with the K promoter is important for the stabilization of Co_2C. Notably, co-feeding 2 volume % of H_2O accelerates the carburization by enhancing the formation of surface carboxylate, which prefers to further split for following C permeation. The K promoter also endows the adsorption of C atoms on the CoO surface, favoring the subsequent carburization. CO_2 converts to C_{2+} HCs via CO^* intermediate derived from carbonate splitting on K-Co_2C catalyst, and a selectivity to C_{2+} HCs up to 67.3% is achieved at 300°C, 3.0 MPa. Furthermore, H_2O (0.5 volume %) is applied to inhibit the decomposition of surface Co_2C and markedly prolongs the catalyst lifetime from 35 to over 200 hours. This work reveals a unique promoting role of H_2O in Co_2C-catalyzed CO_2 hydrogenation and provides a mechanistic understanding of the formation and evolution of Co_2C. It is expected to advance the application of Co_2C in CO_2 hydrogenation, and potentially other reactions.

RESULTS AND DISCUSSION
Synthesis, catalytic performance, and kinetics
As displayed in Fig. 1A, Co_3O_4 and K-modified Co_3O_4 precursors were prepared via a citric acid–induced sol-gel method and subsequent incipient wetness impregnation (IWI) using the solution of K_2CO_3 (0.98 wt %; details in Materials and Methods). XRD patterns and thermogravimetric analysis (TGA) results confirm that the foamy gels were completely decomposed to Co_3O_4 after the calcination at 450°C (fig. S1). The transmission electron microscopy (TEM) and high-resolution TEM (HRTEM) images on Co_3O_4 and K-Co_3O_4 illustrate that there is no substantial change in the average particle size (21 to 24 nm, beyond the sensitive size range in CO_2 hydrogenation) and morphology of Co_3O_4 with the K modification (fig. S2). The particle size of K-Co_3O_4 exhibits a narrower distribution owing to the secondary calcination. Energy-dispersive spectroscopy (EDS) mappings confirm that the K promoter is uniformly dispersed across the Co_3O_4 surface (fig. S3). These precursors were used in CO_2 hydrogenation reaction at 300°C, 3.0 MPa with a space velocity of 6000 ml g^{-1} $hour^{-1}$. We collected the spent samples, which were tested for 3 hours of CO_2 hydrogenation, after careful passivation. The characteristic XRD peaks for spent samples derived from Co_3O_4 and K-Co_3O_4 are assigned to the phases of metallic Co (Co^0), which consists of face center cubic–Co and hexagonal closest packed (hcp)–Co, and Co_2C, respectively (these two spent samples are denoted as Co^0-t and K-Co_2C, respectively) (Fig. 1A). It indicates that these two phases were in situ generated under the reaction conditions.

Some differences in the catalytic performance were observed on Co^0-t and K-Co_2C. As shown in Fig. 1B, K-Co_2C offers a selectivity to C_{2+} HCs of 46.5%, whereas it is only 6.0% on Co^0-t. High-value

products $C_2 \sim C_4^=$ and C_{5+} occupy 13.4 and 16.5% of K-Co_2C with an olefin/paraffin (O/P) ratio of 0.8 and a chain growth factor α of 0.53. In contrast, methane dominates (selectivity as 94.0%) on Co^0-t, while ethane is the only C_{2+} product. The normalized space-time yields (STYs) of C_{2+} HCs based on catalyst mass and surface area reach 7.7 mmol g_{cat}^{-1} $hour^{-1}$ and 0.31 mmol m^{-2} $hour^{-1}$ on K-Co_2C sample, while those on Co^0-t are 1.7 mmol g_{cat}^{-1} $hour^{-1}$ and 0.08 mmol m^{-2} $hour^{-1}$, respectively. We further modulated the K content and found that only K-Co_2C (K fraction as 0.98 wt %) delivered a moderate conversion (38.2%) and high selectivity and STY to C_{2+} HCs, while 0.49% K-Co_3O_4 and 1.96% K-Co_3O_4 samples only yield 2.2 and 1.8 mmol g_{cat}^{-1} $hour^{-1}$, respectively (Fig. 1C and table S1). Further investigations on Na- and Cs-modified samples show decreased selectivity to C_{2+} HCs of 37.0 and 42.8%, while their STYs are 6.4 and 5.9 mmol g_{cat}^{-1} $hour^{-1}$, respectively. In addition, the reaction temperature and pressure on K-Co_2C were optimized (table S2). We found that both CO_2 conversion and CH_4 selectivity increase with the temperature (260° to 340°C), indicating that a high-reaction temperature promotes the CO_2 activation but also boosts the deep hydrogenation to CH_4. The optimum yield to C_{2+} HCs and those to $C_2 \sim C_4^=$ and C_{5+} (2.2 and 2.7 mmol g_{cat}^{-1} $hour^{-1}$) were obtained at 300°C (fig. S4). Tests at various pressures show that the CO_2 conversion and C_{2+} HCs selectivity monotonically increase with the reaction pressure, whereas CO selectivity decreases (fig. S5A). Under pressurized conditions (0.8 to 3.0 MPa), more C_{2+} HCs were detected (above 34.5%), and all the spent samples show well-defined reflections of Co_2C. In contrast, the sample evaluated at atmospheric pressure (0.1 MPa) consists of CoO and Co_2C, while CO is the dominant product (61.8%), revealing that the reaction pressure affects the carburization and C—C coupling (fig. S5B). Considering that Co_2C tends to decompose to Co^0 at a high temperature (above 260°C) and a high pressure (above 2 MPa) in CO-FTS (29), this in situ synthesized K-Co_2C catalyst operated at 300°C and 3.0 MPa extends its application in catalytic CO_2 conversion.

To inhibit the deep hydrogenation of the C_1 intermediate and increase the proportion of valuable C_{2+} HCs, we further optimized the H_2/CO_2 ratio to 2/1. At a comparable conversion (24.2 and 21.6%), Co^0-t (42,000 ml g^{-1} $hour^{-1}$) and K-Co_2C (4500 ml g^{-1} $hour^{-1}$) exhibit the selectivity to C_{2+} HCs as 3.3 and 67.3%, respectively (Fig. 1D). The selectivity to $C_2 \sim C_4^=$ and C_{5+} on K-Co_2C reach 31.6 and 28.7% with an O/P ratio of 4.5. The detailed distribution of C_{2+} HCs is shown in fig. S6 and table S3. The decreased space velocity and H_2/CO_2 ratio favor the carbon chain growth (α of 0.59) and inhibit the rehydrogenation of olefins, leading to a higher proportion of valuable $C_2 \sim C_6^=$. Kinetic analysis was conducted at high space velocities to get insights on enhanced C_{2+} HCs generation on K-Co_2C. The apparent activation energies (E_a) for CH_4 and C_{2+} HCs generation were estimated as 96.7 ± 4.1 kJ mol^{-1} and 50.1 ± 1.5 kJ mol^{-1} on K-Co_2C versus 80.4 ± 4.6 kJ mol^{-1} and 92.9 ± 4.8 kJ mol^{-1} on Co^0-t, revealing that C_{2+} HCs formation is more facile, whereas CH_4 formation is inhibited on K-Co_2C (Fig. 1, E and F). Apparent reaction orders on K-Co_2C (CO_2 $α_1 = 0.48 ± 0.03$ and H_2 $β_1 = 0.98 ± 0.05$) and Co^0-t (CO_2 $α_2 = 0.88 ± 0.01$ and H_2 $β_2 = 0.32 ± 0.02$) further evidence that the enhanced CO_2 or suppressed H_2 activation profit the C_{2+} HCs formation instead of CH_4 on K-Co_2C (Fig. 1G) (30). Moreover, compared with K-Co_2C, the similar CO_2 reaction order ($α_3 = 0.47 ± 0.01$) and the evidently increased H_2 reaction order ($β_3 = 1.34 ± 0.04$) of 1.96% K-
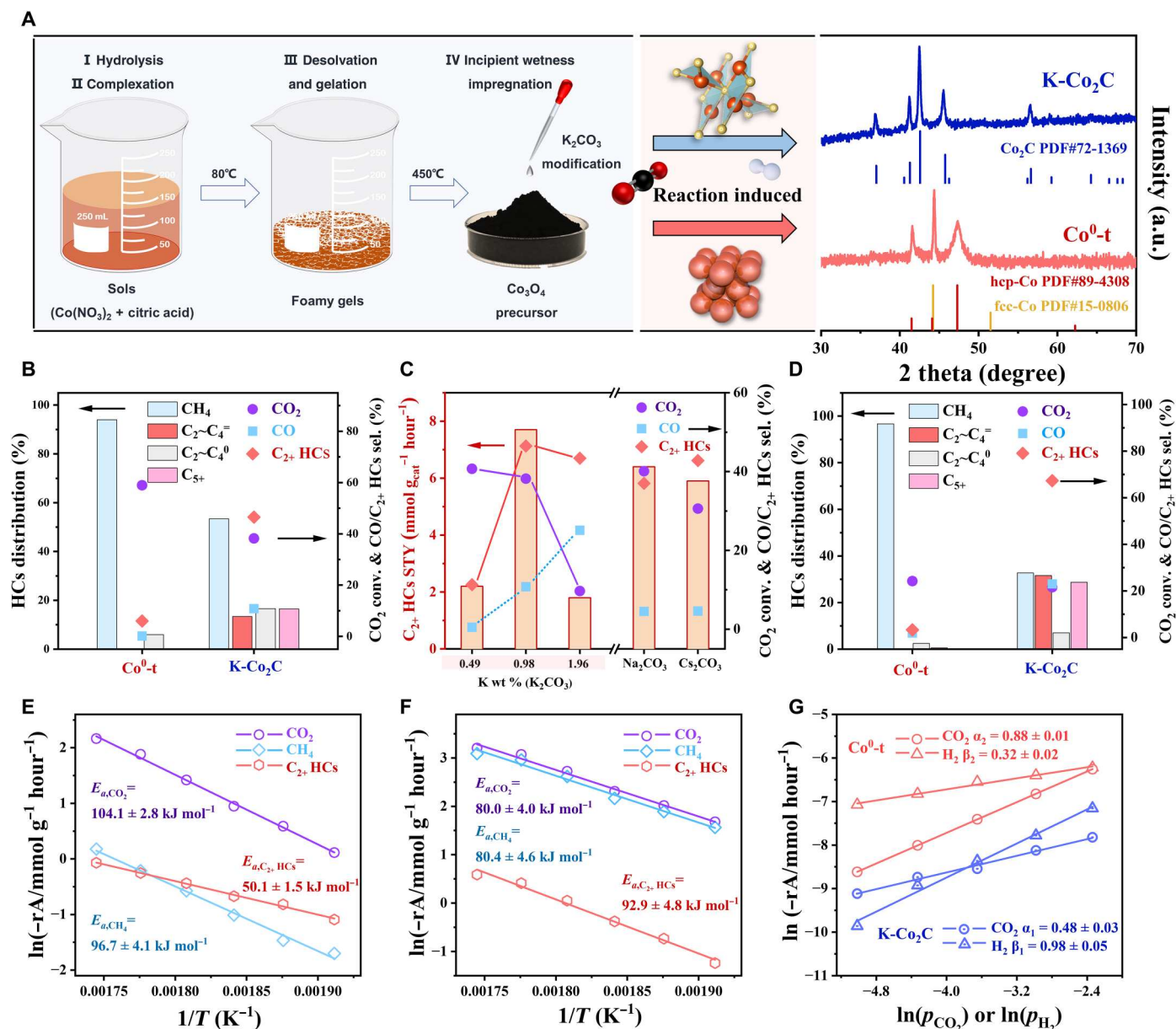
Fig. 1. Catalyst synthesis and catalytic properties. (**A**) Scheme for the reaction-induced in situ synthesis and XRD patterns of K-Co_2C and Co^0-t samples. (**B**) Catalytic performance on Co^0-t and K-Co_2C at 300°C, 3.0 MPa, space velocity = 6000 ml g^{-1} hour^{-1}, H_2/CO_2 = 3. (**C**) C_{2+} HCs space-time yield (STY) and catalytic performance for adjusted K loadings and alkali metal promoters at the same reaction conditions. (**D**) Catalytic performance at optimized reaction conditions, Co^0-t: H_2/CO_2 = 2, 42,000 ml g^{-1} hour^{-1}; K-Co_2C: H_2/CO_2 = 2, 4,500 ml g^{-1} hour^{-1}. (**E**) Activation energies for CO_2 conversion and C_{2+} HCs or CH_4 formation on K-Co_2C. (**F**) Activation energies on Co^0-t sample. (**G**) CO_2 and H_2 reaction orders evaluated at 260°C, 3.0 MPa. wt %, weight %; a.u., arbitrary units.

Co_3O_4 (fig. S7) suggest that the excessive K promoter inhibits the H_2 activation, instead resulting in the declined catalytic performance. We further investigated the specific properties of CO_2 and H_2 adsorption and activation on Co_2C and Co surfaces using density functional theory (DFT) calculations. Compared with Co, the CO_2 adsorption and dissociation energies on the Co_2C surface decreased from −0.08 to −0.26 eV, and −1.19 to −1.57 eV, respectively (fig. S8A). Thus, CO_2 adsorption and activation are enhanced on Co_2C. There is essentially no difference between the molecular adsorption energies of H_2 on the two surfaces (fig. S8B). However, the dissociation energy of H_2 on the Co surface (−1.22 eV) is

exothermic, whereas the dissociation energy on Co_2C (0.04 eV) is energetically less favorable.

Structural characterization

The specific surface areas of Co^0-t and K-Co_2C are 20.9 and 24.8 m^2 g^{-1} (table S4), and their average particle sizes are 23.2 ± 0.1 and 26.6 ± 0.2 nm as estimated from the XRD results, respectively. TEM and representative HRTEM images show that K-Co_2C represents a cylindrical morphology. The interplanar distances of 0.200, 0.218, and 0.243 nm match the (210), (020), and (101) planes of Co_2C, respectively (Fig. 2, A to C) (31). We verified that the K promoter is still
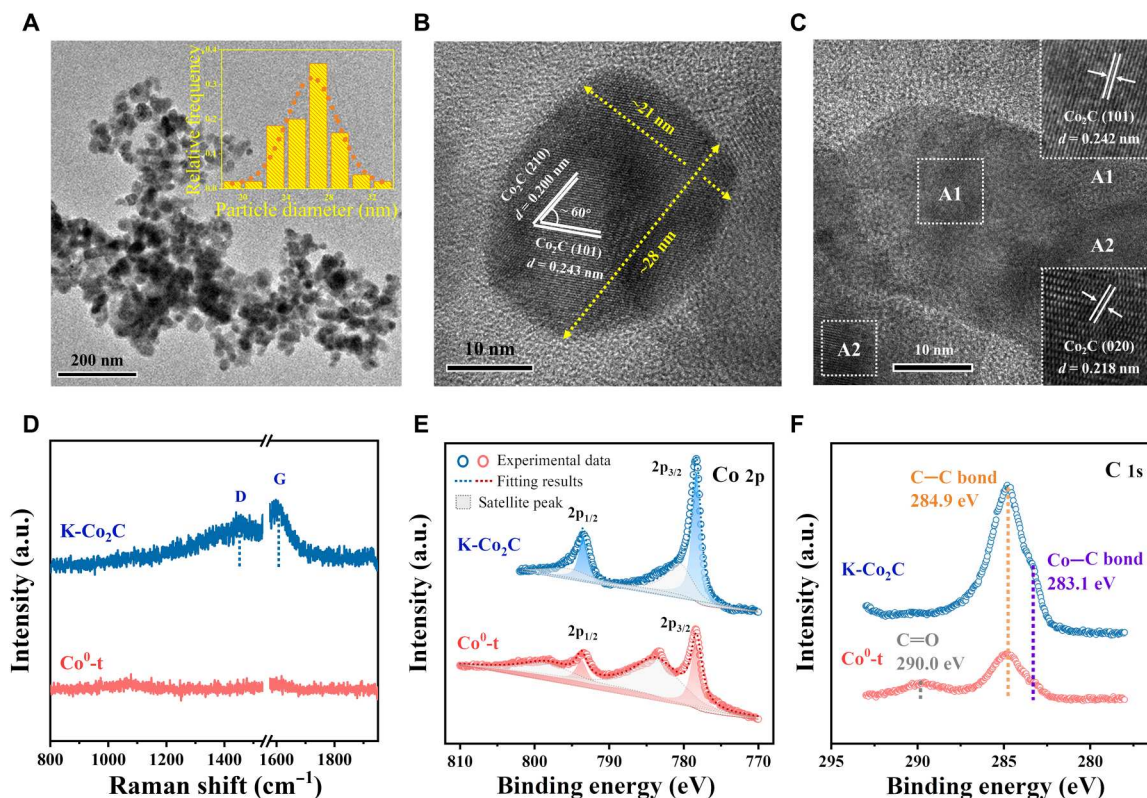
Fig. 2. Structural characterizations of spent catalysts. (**A**) TEM images and particle size distribution of K-Co$_2$C. (**B** and **C**) HRTEM images of K-Co$_2$C. (**D**) Ultraviolet Raman spectra of K-Co$_2$C and Co^0-t. Quasi in situ x-ray photoelectron spectroscopy (XPS) spectra of K-Co$_2$C and Co^0-t (**E**) Co 2p spectra and (**F**) C 1s spectra.

uniformly dispersed on the Co$_2$C surface (fig. S9), suggesting that there is no obvious migration or agglomeration of K during the reaction. As for Co^0-t, the (002) and (100) planes of hcp-Co were clearly observed (fig. S10). Previous DFT results by Zhang *et al.* (*32*) suggest that (101) and (020) facets of Co$_2$C compete for CH$_x^*$ coupling, leading to the high selectivity to C$_{2+}$ HCs on K-Co$_2$C. Ultraviolet (UV) Raman spectroscopy (Fig. 2D) with a 320-nm laser was used to probe the information of C species at about 10 nm in depth without the interference of fluorescence (*33*). Two Raman shifts observed on K-Co$_2$C of ~1453 and ~1606 cm^{-1} are ascribed to the D and G bands of C species in Co$_2$C, which represents the A$_{1g}$ vibration of disordered graphite and E$_{2g}$ vibration of graphitic carbon, respectively (*21*, *34*). The I_D/I_G value (calculated using the deconvoluted peak area) for K-Co$_2$C is ~1.38, suggesting the low disorder degree and surface energy (*21*). In contrast, no signal was detected on the metallic Co^0-t sample.

Considering the carbide is sensitive to air, the surface properties of spent catalysts were further investigated using quasi in situ x-ray photoelectron spectroscopy (XPS) without exposure to air. The K 2p features of K$^+$ species in K$_2$CO$_3$ were observed at 296.8 and 294.2 eV on K-Co$_2$C (fig. S11) (*35*). The binding energies of Co 2p$_{1/2}$ and 2p$_{3/2}$ in Co$_2$C (793.5 and 778.3 eV on K-Co$_2$C) and Co^0 (793.6 and 778.4 eV on Co^0-t) are similar, except for the signals at 798.0 and 783.5 eV associated with the superposition of Co^0 satellite peaks and Co^{2+} 2p peaks (Fig. 2E) (*36*). The Co$_2$C species on the surface of K-Co$_2$C was also identified according to the signal of the C 1s band at 283.1 eV, assigned to the Co—C bond (Fig. 2F). The characteristic peaks of the C=O group and the C—C bond

originated from the surface adsorbed species appear at 290.0 and 284.9 eV, respectively (*22*). The surface C/Co molar ratio, which was estimated on the basis of the deconvoluted results, on K-Co$_2$C (0.27) is much higher than that on Co^0-t (0.12), suggesting the enhanced carburization with K modification.

Adsorption properties and reaction mechanism

Temperature programmed desorption (TPD) of CO$_2$, CO, and H$_2$ combined with online mass spectrometry (MS) was performed to characterize the adsorption properties (fig. S12). Compared with Co^0-t, K-Co$_2$C shows an enhanced medium-strong adsorption of CO$_2$ and CO (300° to 450°C), but a diminished adsorption of H$_2$. The medium-strong adsorbed CO$_2$ and CO species on K-Co$_2$C, which is more inclined to be activated and involved in the subsequent conversion, can create a relatively C-rich and H-lean environment, inhibiting the deep hydrogenation while promoting the C—C coupling (*37*). In situ diffuse reflectance infrared Fourier transform spectroscopy (DRIFTS) was carried out to gain insight into the reaction pathways, and the detailed peak assignments are listed in table S5. As shown in Fig. 3A, the spectra for CO$_2$ pre-adsorbed on K-Co$_2$C were collected during the pressurization of CO$_2$ to 1.2 MPa at 50°C and subsequent heating to 260°C. CO$_2$ was initially activated as monodentate carbonate (m-CO$_3^{2-}$, at 1511, 1437, 1395, and 1278 cm^{-1}) and bidentate carbonate (b-CO$_3^{2-}$, at 1676 and 1625 cm^{-1}) on the K-Co$_2$C surface (*38–41*). The features of adsorbed CO (CO$_{ads}$) on Co$_2$C (2078 cm^{-1}) and Co^0 (2059 cm^{-1}) were detected once the pressure was increased to 0.6 MPa, and that of bicarbonate (HCO$_3^-$, at 1606 cm^{-1}) emerges at 200°C, 1.2 MPa,
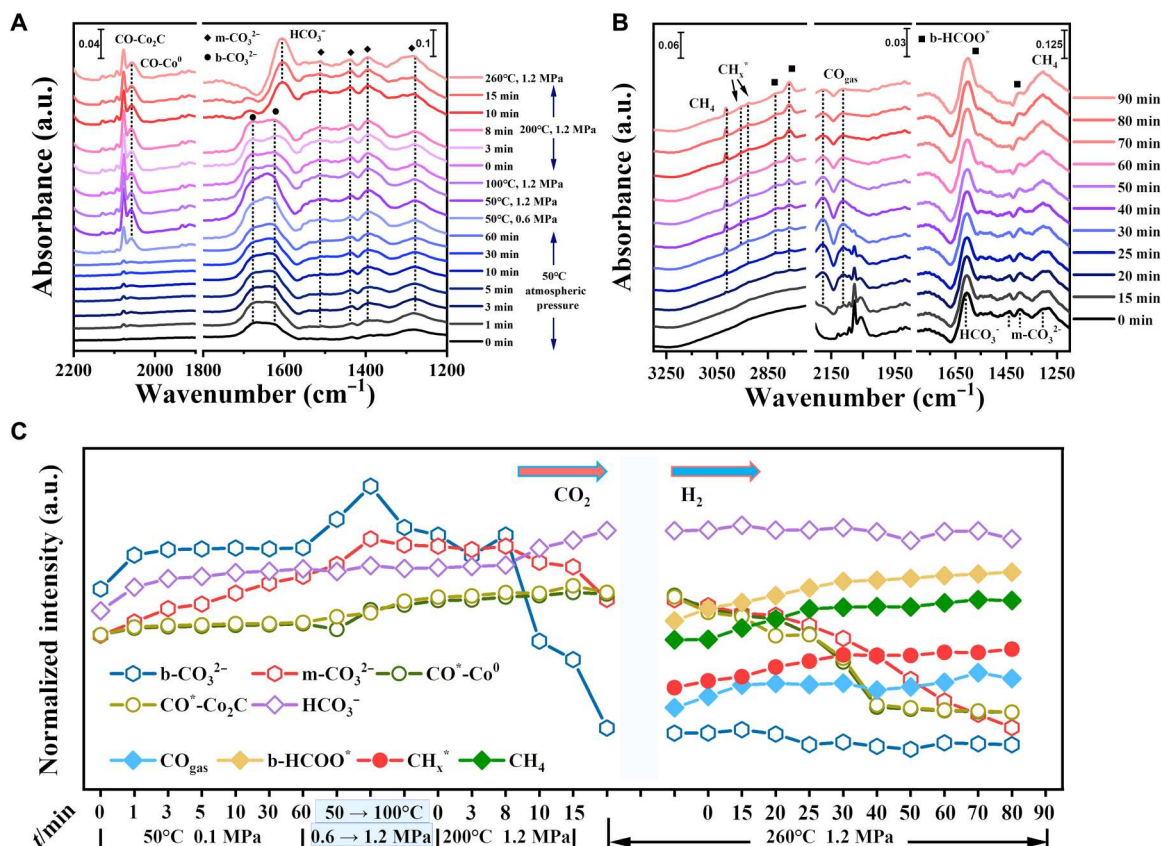
Fig. 3. Reaction mechanism studies. In situ DRIFTS spectra on K-Co₂C for (**A**) CO_2 pre-adsorption. (**B**) Intermediates conversion with switching to H_2 at 260°C, 1.2 MPa. (**C**) Evolution of surface species according to the intensity of infrared featured bands.

indicating that the residual H species originated from the pretreatment or the hydroxyl group assists in the surface reaction (*38*). This CO_{ads} species reveals that, on the K-Co₂C surface, a small amount of CO_2 preferentially converted to CO at mild conditions (*38*). After switching to H_2 (Fig. 3B and fig. S13A), the features of bidentate formate (b-HCOO*, the stretching and bending vibrations of C—H band at 2766, 2680, and 1400 cm^{-1}, and the vibration of OCO group at 1591 cm^{-1}) and that of generated gaseous CO (CO_{gas}, at 2178 and 2111 cm^{-1}) and CH_4 (3015 and 1306 cm^{-1}) and the vibrations of C—H bonds in C_{2+} HCs as CH_3 (2956 cm^{-1}) and CH_2 (2929 cm^{-1}) (the enlarged spectra are shown in fig. S13B) were observed (*39*, *42*). The varying tendency of above species as determined by the featured peak (table S6) intensity with time is shown in Fig. 3C. It can be seen that the CO_3^{2-} rapidly reduces starting at 50°C, 1.2 MPa with an increasing intensity of CO_{ads}, indicating that CO_3^{2-} initially converts to CO_{ads} without the H assistance. Surface HCO_3^- has gradually accumulated and reaches a steady state after 260°C, 1.2 MPa. The introduction of H_2 results in the reduction of CO_{ads} and m-CO_3^{2-} with an increase of CH_x^* from 0 to 30 min and continuous generation of CO_{gas} and HCs. Moreover, the intensity of b-HCOO* increases after H_2 addition but its further conversion is not observed. It is speculated that CO_{ads} derived from CO_3^{2-} is an important intermediate for CH_x^* generation, which is further coupled to C_{2+} HCs on K-Co₂C catalyst, whereas the HCO_3^- and b-HCOO* seem acting as spectators. By comparison, as for Co⁰-t catalyst (figs. S14 and S15),

the intensities of b-HCOO* rapidly decreased after switching to H_2, while those of monodentate formate (m-HCOO*) and product CH_4 simultaneously increased, indicating that the generation of CH_4 mainly undergoes the b-HCOO*−mediated pathway. Moreover, the signal of CO_{ads} also emerged during CO_2 adsorption (200° to 260°C) and quickly vanished after the H_2 introduction. It reveals that the CO_{ads} species is also possibly involved in the CH_4 formation.

In situ synthesis and stabilization of Co₂C

We resorted to in situ XRD and theoretical calculations to shed light on the structural evolution of Co-species during the reaction. The reduction properties were first determined as discerned by the in situ XRD patterns of as-prepared Co_3O_4 and K-Co_3O_4 in H_2 (fig. S16). We found that K addition increased the complete reduction temperature from 300° to 360°C, suggesting that, to some extent, it inhibits the reduction of cobalt oxide toward the Co⁰. Under the CO_2 hydrogenation atmosphere (Fig. 4A), the Co_3O_4 modified with K was first reduced to CoO and then carburized to Co₂C at 260°C within 2 hours, and the reflection of Co⁰ was absent throughout the test. In combination with the semiquantitative XPS analysis (Fig. 2, E and F) that the surface C/Co ratio (0.27) on K-Co₂C is relatively lower than the standard stoichiometric coefficient in Co₂C (0.50), we speculate that, with K modification, the Co₂C was in situ generated, followed by its partial decomposition to Co⁰ on the catalytic surface. Regarding that Co⁰ species generally
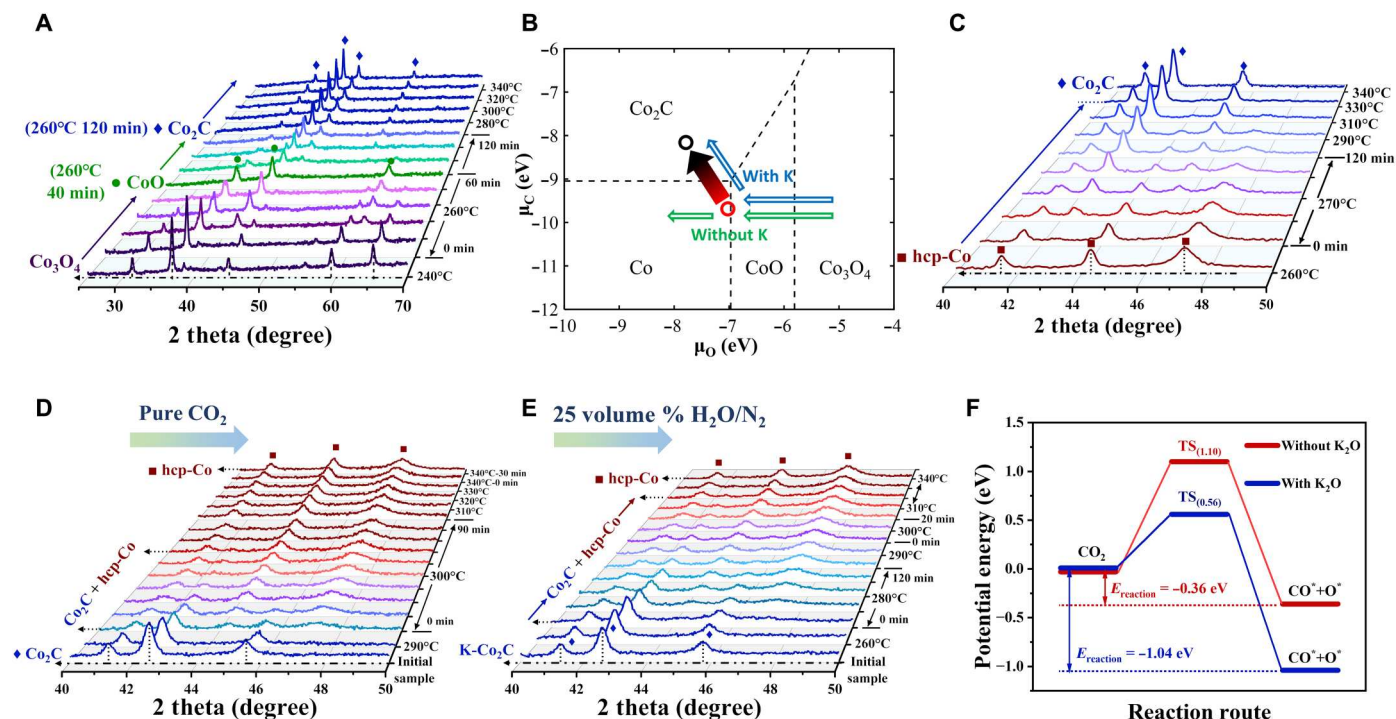
Fig. 4. Structural evolutions and theory calculations. (**A**) In situ XRD patterns of K-Co_3O_4 in CO_2 hydrogenation at 0.8 MPa. (**B**) Phase diagram of Co-O-C trinary system derived from the DFT energies of bulk crystals. (**C**) In situ XRD patterns of K-Co^0 sample in CO_2 hydrogenation at 0.8 MPa; the K-Co^0 sample was synthesized from the decomposition of K-Co_2C in H_2 at 340°C, 0.8 MPa. In situ XRD patterns of K-Co_2C (**D**) in pure CO_2 at 0.8 MPa, (**E**) in 25 volume % H_2O/N_2 at 0.1 MPa. Potential energy profiles. (**F**) CO_2 dissociation to CO^* and O^* on Co_2C (101) surface with or without K_2O.

participates in deep hydrogenation to CH_4, a strategy against this decomposition is still required. In comparison, the Co_3O_4 without K was reduced to CoO and then directly to Co^0 at 260°C within 50 min (fig. S17 and green arrows in Fig. 4B). Ab initio thermodynamics methods were applied to derive the phase diagram and depict the structural evolution of the catalyst. The chemical potentials for C (μ_C) and O (μ_O) are determined according to the gas-phase composition and reaction conditions (*43*). As displayed in Fig. 4B, the initial reaction condition is located at the red circle ($\mu_O = -7.02$ eV, $\mu_C = -9.69$ eV) which is near the computed boundary of the CoO phase. This μ_O value is below the Co_3O_4 phase. Therefore, once Co_3O_4 is exposed to the environment, a reduction in the CoO will occur. During the reaction, μ_O decreases, while μ_C increases due to the CO generated from CO_2 reduction. As a result, the final chemical potentials migrate to the black circle ($\mu_O = -7.79$ eV, $\mu_C = -8.16$ eV), which is inside the domain of Co_2C, suggesting that its formation from CoO is thermodynamically favorable under reaction conditions. Considering that the Gibbs free energy change (ΔG) is more negative for the carburization from CoO than that from Co^0 (fig. S18), and no bulk Co^0 was observed during the evolution (Fig. 4A), we speculate that the thermodynamic advantages directly propel CoO into carburization without the reduction to Co^0. We then investigated the structural evolution in CO_2 hydrogenation for the K-Co^0 sample, which was obtained from the decomposition of K-Co_2C. The in situ carburization of metallic cobalt toward Co_2C was also observed, exhibiting the gradually increased C_{2+} HCs selectivity and reduced CH_4 selectivity along with the reaction (fig. S19). The CH_4 dominates in the initial products of K-Co^0 [time on stream (TOS) = 1 hour] or Co^0-t samples, suggesting

that the introduction of the K promoter does not substantially influence the product selectivity. The temperatures for the emergence of Co_2C reflections and the disappearance of Co^0 reflections increase to 270° and 330°C, respectively (Fig. 4C), suggesting that the synthesis of Co_2C from Co^0 precursor requires a high temperature for the C permeation into the Co lattice. We are thus confident that the in situ synthesis of Co_2C in CO_2 hydrogenation starts from K-modified CoO (blue arrows in Fig. 4B) instead of Co^0. By comparison, the syngas preferentially induces the reduction to Co^0, while the following carburization originates from Co^0 (*16*). The replacement of CO with CO_2 results in an increased μ_O, favoring the unique CoO route for the synthesis of Co_2C. Moreover, this oxide-mediated carburization is different from that of iron catalysts although their carbides have many similarities. Metallic iron is more advantageous than its oxide for the formation of FeC_x, and this key difference is helpful to understand the distinct evolution and deactivation pathways for cobalt- and iron-based catalysts in CO_x conversion (*44, 45*).

Structural stability is a key factor for catalysts. As evidenced by the in situ XRD patterns in N_2 at 0.8 MPa (fig. S20), K-Co_2C is thermally stable below 340°C without bulk decomposition. Its stability in the presence of reactants and products is also important but still uncertain. Co_2C is considered a metastable phase under the H-rich environment, and, from the in situ XRD results of K-Co_2C in pure H_2, it can be clearly seen that the transition of Co_2C to Co^0 occurs at 290°C (fig. S21). A recent report has proven that CO_2 adsorbs on the surface as carboxylate ($CO_2^{\delta-}$) and then splits to C^* in the presence of H_2, enabling the following C permeation (*22*). We performed the in situ XRD investigations on K-Co_2C in pure CO_2 and found that

excessive CO_2 also removes the C from Co_2C at 300°C (Fig. 4D). Previous results have shown that H_2O can oxidize hcp-Co to CoO or cobalt hydroxide but its effect on Co_2C is unclear (46). We investigated the evolution of K-Co_2C in 25 volume % (the theoretical value of volume fraction and the same as below) H_2O/N_2 and found that excessive H_2O causes the transition of Co_2C to hcp-Co in the range of 280° to 310°C (Fig. 4E). There is no obvious oxidation in bulk below 340°C, possibly originated from the fast O^* removal with K-promoting effect (47). When the H_2O content was decreased to 5%, this transition intensively occurred in the temperature region of 330° to 340°C (fig. S22), which is higher than that with co-feeding 25% H_2O, implying that the H_2O concentration also has an impact on the decomposition of Co_2C. Inspired by the above findings, we believed that the single reactant or product (H_2O) of high concentrations could destroy the K-Co_2C but a unique balance between them in CO_2 hydrogenation presents an opportunity for its stabilization. We further inquired into the effect of the K promoter. We prepared a Co_2C sample without K (denoted as Co_2C-t) through a reduction-carburization procedure from Co_3O_4. However, it rapidly decomposed to hcp-Co at 260°C in CO_2 hydrogenation within 20 min as confirmed by the in situ XRD results (fig. S23). Moreover, the DFT results on the Co_2C (101) surface reveal that with the modification using the K_2O promoter, the direct splitting of CO_2 to CO is more facile, considering that the energy barrier and energy of reaction ($E_{reaction}$) reduce from 1.10 to 0.56 eV and −0.36 to −1.04 eV, respectively (Fig. 4F). Since CO_2 is adverse to the stabilization of Co_2C whereas CO enhances the carburization, the promoting effect on CO_2 direct dissociation here is also important for stabilizing the Co_2C. Hence, we reveal that the reaction atmosphere in conjunction with the K promoter is crucial in the stabilization of Co_2C.

H_2O promoted carburization and stabilization

Since H_2O is a common impurity for CO_2 capture and more H_2O is generated in CO_2-FTS compared with CO-FTS, we further delve into its influences on the carburization and the catalytic reaction. We simulated the carburization from K-CoO in 10% CO/N_2 and, as shown in Fig. 5A, in situ XRD results demonstrate that the transformation of CoO to Co_2C started at 260°C and finished at 280°C as evidenced by the vanishing CoO feature at 36.5°. While 2% H_2O was co-fed (at 0.1 MPa, Fig. 5B), despite the constant temperature for the beginning of carburization at 260°C, the transition of CoO to Co_2C was accomplished at 270°C. Once the H_2O content was increased to 5%, the onset and end temperatures for the carburization shifted to 290° and 300°C, respectively (fig. S24). As stated above, a moderate amount of H_2O facilitates the carburization of K-CoO and reduces the carburizing temperature, while its content is crucial. Most previous studies reported the negative effect of H_2O on the active centers, including the induced oxidation or sintering of Co^0 nanoparticles (48–50). So far, the promoting effect of H_2O on the carburization to Co_2C has never been reported to the best of our knowledge.

To obtain more evidence on the catalytic surface, we collected the quasi in situ XPS spectra in the NAP-XPS system during the carburization of K-CoO. As shown in the Co 2p spectra (Fig. 5, C and D), the characteristic peaks at 780.3 and 796.4 eV and their satellite features at 786.3 and 802.9 eV are attributed to the divalent Co species in the octahedral site of CoO (51). In 10% CO/N_2, the features of CoO kept almost unchanged, while only a faint signal of

Co—C bond was first detected at 300°C, inferring a slight surface carburization of K-CoO (Fig. 5C). However, by co-feeding 2% H_2O, the peak of Co—C bond (283.0 eV) initially emerged at 250°C, and then gradually developed with the increasing temperature (Fig. 5D). Meanwhile, the featured Co 2p peaks completely shifted from CoO (780.0 eV) to Co_2C (778.1 eV) at 300°C, illustrating the full carburization of the surface. These results explicitly verify the promoting effect of H_2O in the carburization of K-CoO. Furthermore, for the fresh K-CoO sample, the K $2p_{1/2}$ and $2p_{3/2}$ peaks at 295.2 and 292.7 eV are associated with K^+ species in K_2O (52). With the increasing temperature in CO or CO + H_2O flow, these characteristic peaks gradually shifted to high binding energies and lastly reached at 295.7 and 293.0 eV at 300°C, revealing that the surface K_2O species reacted with the CO to form carbonate.

To gain insight into this promotion, we contrasted the interaction between CO and pristine CoO surface with and without H_2O. As shown in the quasi in situ XPS spectra, the surface CoO (780.2 eV) was fully reduced to Co^0 (778.5 eV) at 300°C in 10% CO, while co-feeding 2% H_2O prevents this reduction (Fig. 6A). For C 1s spectra (Fig. 6B), a shoulder peak at ~288.0 eV assigned to surface C—O species, including the possible CO_3^{2-}, HCO_3^-, and $CO_2^{\delta-}$, appears with H_2O addition. These adsorbed species were further determined by in situ DRIFTS. The spectra collected at 1 and 30 min are used for probing the initial and final adsorbed species, respectively, while the changing processes are recorded in figs. S25 and S26. As shown in Fig. 6C, for the CoO-t sample in 10% CO, the initial peaks at 1609, 1509, and 1268 cm^{-1} correspond to b-CO_3^{2-} adsorbed on the CoO surface and those at 1366 and 1318 cm^{-1} correspond to polydentate carbonate (p-CO_3^{2-}) species (40). Along with the surface reduction (fig. S25), some adsorbed species gradually shift to HCO_3^- (1604 cm^{-1}, H is from surface hydroxyl) and m-CO_3^{2-} (1463, 1377 cm^{-1}) on Co^0. While 2% H_2O was added, a band at 1438 cm^{-1} and the shoulder peak at 1425 cm^{-1}, which are attributed to the stretching vibration of the C=O band and the bending vibration of the C—H band in formyl (HCO*) species, were observed on the CoO surface (53). The b-CO_3^{2-} and monodentate formate (m-HCOO*, which is identified by the stretching vibrations of the OCO group at 1542 and 1358 cm^{-1}, and the bending vibration of C—H band at 1392 cm^{-1}) were also observed (54). Without K modification, these species mostly convert to adsorbed m-CO_3^{2-}, which is inactive for carburization. As for the K-CoO sample, a signal at 1745 cm^{-1} associated with adsorbed CO on three- or fourfold hollow sites (55) was both observed with and without co-feeding H_2O, suggesting that the K promoter provides additional sites for enhanced CO adsorption, which is in accordance with the CO-TPD-MS results (fig. S12B). In 10% CO, b-HCOO* at 1565 and 1364 cm^{-1}, and m-CO_3^{2-} are initially adsorbed and accumulated, while additional HCO_3^- species (1605 cm^{-1}) was observed at 30 min on the K-CoO surface. Notably, with the addition of 2% H_2O, the bands at 1556, 1415, and 1336 cm^{-1}, which are assigned to the $CO_2^{\delta-}$, were detected (22, 56, 57). With an extension of the treatment time, these species have accumulated in 1 to 10 min and then are gradually consumed along with the surface carburization (fig. S26). The final adsorbed species on a fully carburized surface is HCOO* while physically adsorbed H_2O (1660 cm^{-1}) was also detected. In literature results, compared with HCOO* and CO_3^{2-}, $CO_2^{\delta-}$ is easier to split and form C* species for carburization (22). According to the above XPS and infrared (IR) results,
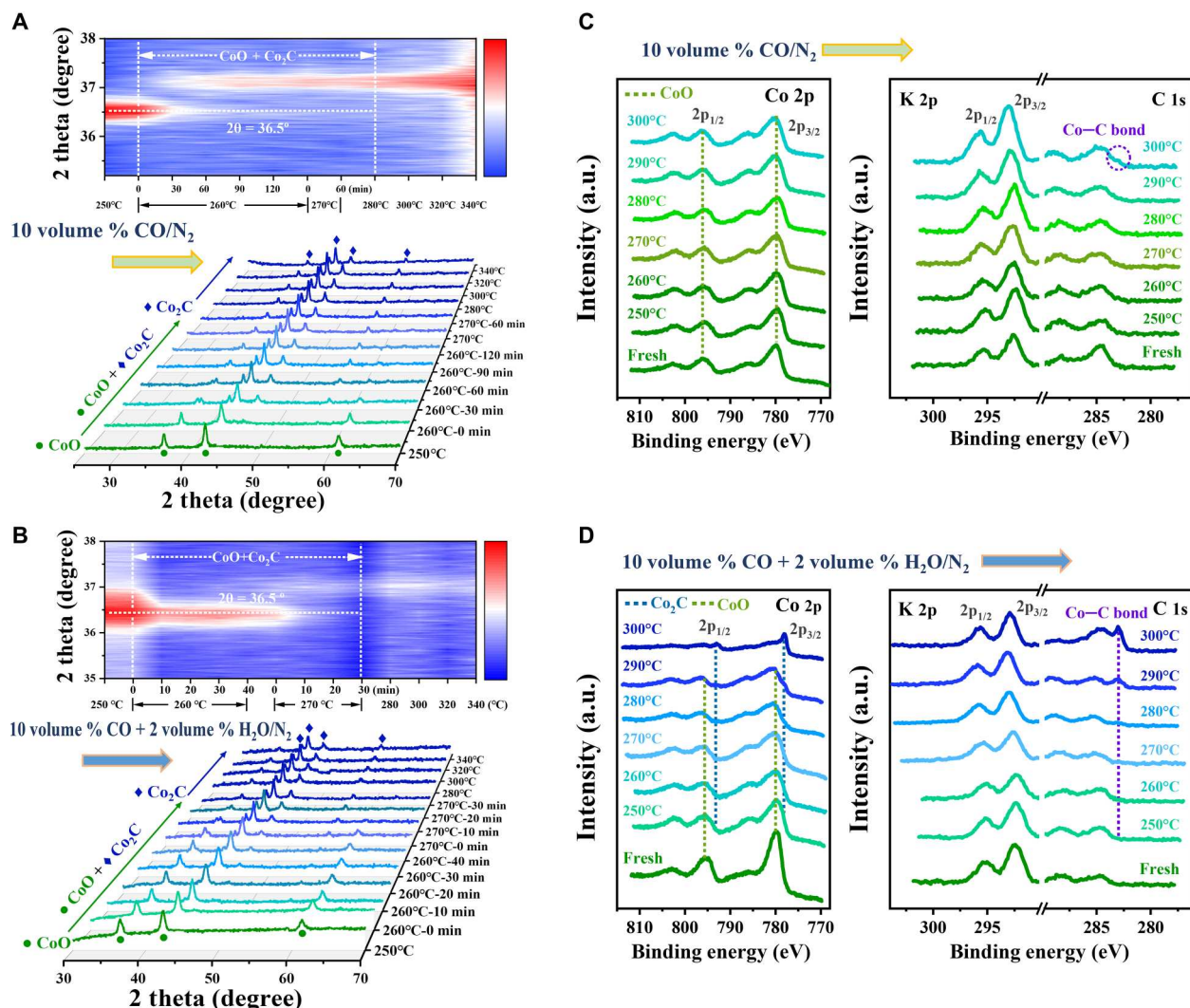
Fig. 5. Facilitating carburization of K-CoO sample with a moderate amount of H$_2$O. In situ XRD patterns recorded (**A**) in 10 volume % CO/N$_2$ at 0.8 MPa and (**B**) in 10 volume % CO + 2 volume % H$_2$O/N$_2$ at 0.1 MPa. Quasi in situ XPS spectra in the near-ambient pressure (NAP) XPS system recorded after reaction at 0.1 MPa (**C**) in 10 volume % CO/N$_2$ and (**D**) in 10 volume % CO + 2 volume % H$_2$O/N$_2$.

we speculate that the promotion originates from the H$_2$O-facilitated formation of surface C—O species, including the HCO* or CO$_2^{\delta-}$ species. However, without the K promoter, the HCO* converts to CO$_3^{2-}$; while only the K promoter and H$_2$O jointly act on the CoO surface, the active CO$_2^{\delta-}$ species can be generated and involved in the subsequent carburization.

We calculated the dissociation of CO$_2^{\delta-}$ (CO$_2^*$) toward C* species on the CoO (200) surface. As demonstrated in fig. S27, with the presence of K$_2$O promoter and H$_2$O, the CO$_2^*$ dissociation energy (reaction I: CO$_2^* \rightarrow$ CO* + O*) declines about 0.7 to 2.07 eV. Notably, the reaction energies for C* formation of reactions II (CO$^* \rightarrow$ C* + O*) and III (CO* + CO$^* \rightarrow$ C* + CO$_2^*$) reduce to 0.67 and −0.54 eV, which are lower than those on clean CoO (6.47 and 3.19 eV) or K$_2$O-CoO (5.45 and 2.47 eV) surfaces. The results show that K$_2$O and H$_2$O jointly promote the dissociation of surface CO$_2^{\delta-}$ to C* species. Besides, after the dissociation of the C—O species to C*, the adsorption of surface C atoms is important for carburization, and we further investigated this process on CoO. The average

number of electrons transferred between C atoms and the CoO surface (described by Bader charge) and the average formation energies of adsorbed C atoms (ΔE_{form}) calculated with and without K$_2$O co-adsorption are summarized in table S7. Two or three C atoms (marked as 2C and 3C) were deposited on the CoO surface to restore the situation of multicarbon co-adsorption. The Bader charges are 2.13 (2C) and 2.16 (3C) on the clean CoO surface. They increase to 2.28 (2C) and 2.22 (3C) in the presence of K$_2$O, indicating that more electrons are transferred from the C atoms to the CoO surface, and that K$_2$O enhances the electronic interaction between C* and the catalyst surface. As a result, with the K$_2$O addition, the ΔE_{form} decreases from 3.69 (2C) and 3.63 eV (3C) to 3.25 (2C) and 3.20 eV (3C), respectively. This reduction in formation energies (exceed, 0.4 eV) demonstrates that the adsorption of C* species on the CoO surface is easier with K$_2$O promotion, which favors C accumulation and permeation to form a bulk carbide. These calculation results agree with the experimental observations that K$_2$O and H$_2$O promote carbide formation.
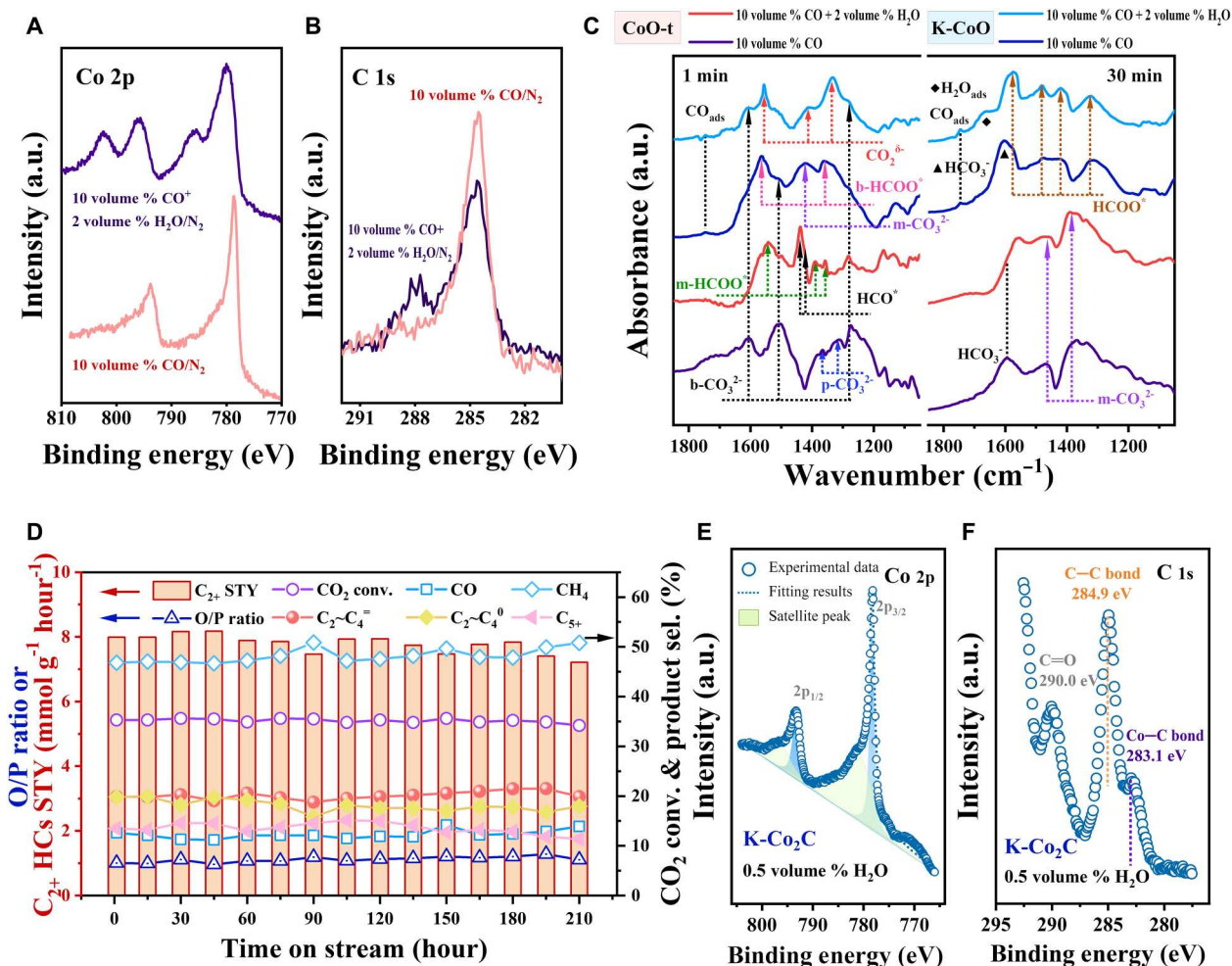
Fig. 6. Effect of co-feeding H_2O on structural properties and catalytic performance. Quasi in situ XPS spectra collected on CoO-t sample after treating in 10 volume % CO with or without co-feeding 2 volume % H_2O (**A**) Co 2p spectra and (**B**) C 1s spectra. (**C**) In situ DRIFTS spectra collected at 1 and 30 min on CoO-t and K-CoO samples under different treated conditions. (**D**) Catalytic stability test with co-feeding 0.5 volume % H_2O within 210 hours. Reaction conditions: 300°C, 3.0 MPa, space velocity = 6000 ml g^{-1} $hour^{-1}$, $H_2/CO_2 = 3$. Quasi in situ XPS spectra of K-Co_2C sample that was used in CO_2 hydrogenation with co-feeding 0.5 volume % H_2O (**E**) Co 2p spectra and (**F**) C 1s spectra.

Given that the surface of K-Co_2C decomposes in the reaction (Fig. 2F), there is a possibility to exploit the beneficial effect of co-feeding H_2O for inhibiting this decomposition and improving the catalytic stability. We first evaluated the effect of co-fed H_2O content on the performance (fig. S28; the data are collected at TOS = 3 hours, while there is no obvious deactivation) and found that when it increases to 0.25 and 0.5%, the CO_2 conversion slightly decreases from 37.9 to 35.6% and 35.3%, respectively. However, more H_2O addition exacerbates the activity declination, while the conversion drops to 24.2% with co-feeding 2.5% H_2O. While the added H_2O content was increased to 25%, the overall CO_2 conversion further dropped to 17.5% and the CH_4 (selectivity as 86.8%) dominates in the products. The generated H_2O in the actual reaction or its extra addition gives rise to the competitive adsorption with other reactants or intermediates and increases the rate of reverse reaction, which jointly causes a gradually reduced CO_2 conversion (*28*). Moreover, a volcanic curve was observed for C_{2+} HCs selectivity and yield with H_2O content, and at the optimum content of 0.5%, the C_{2+} HCs selectivity increases to 53.1% and its STY of

C_{2+} HCs is 8.0 mmol g^{-1} $hour^{-1}$. As can be seen from the C_{2+} HCs composition (fig. S29), co-feeding 0.5% H_2O leads to a more centralized product distribution (α decreases from 0.53 to 0.48) and an enhanced generation of light olefins (the $C_2 \sim C_4^=$ selectivity increases to 19.9% and O/P ratio increases to 1.0), indicating that co-feeding 0.5% H_2O here protects the surface Co_2C from decomposition. Moreover, in CO-FTS, H_2O sometimes promotes the formation of CH_x^* species via an H_2O-assisted methylidyne mechanism and increases the C_{5+} selectivity (*58*). However, a slightly decreasing C_{5+} selectivity was observed with H_2O addition here. It is speculated that the low concentration of H_2O (0.5% ~ 2.5%) does not substantially influence the reaction pathway but is enough to modulate the surface compositions. The promoting effect of H_2O on stabilizing the structure of Co_2C and its catalytic features is expected to enable its practical application in the CO_2 hydrogenation reaction with high temperature and pressure.

The catalytic stability of K-Co_2C in CO_2 hydrogenation was examined, as shown in figs. S30 and S31, we found that the H_2O content has an impact on the catalyst deactivation. Within the

initial 35 hours, without co-feeding H_2O, the CO_2 conversion and C_{2+} HCs selectivity decreased from 38.2 to 31.6% and 46.5 to 38.8%, respectively. The addition of H_2O effectively inhibited this activity decline, and when co-feeding 0.5% or more H_2O, the catalytic performance basically kept stable in the initial 35 hours. We further compared the changes in catalytic performance with various H_2O contents (fig. S32). The drops of C_{2+} HCs STY can be clearly observed when the H_2O content is 0 or 0.25%. As for the H_2O content of 0.5 ~ 2.5%, the ratios of CO_2 conversion collected at 3 and 35 hours (ratio A) and those of C_{2+} HCs STY (ratio B) are all in the range of 96 to 98%, which are higher than those recorded at 0 or 0.25% H_2O. It reveals that co-feeding H_2O is beneficial to mitigating the deactivation, and when the H_2O content exceeded 0.5%, the features of deactivation are quite similar. Furthermore, without co-feeding H_2O, the decrease of the activity (31.6 to 24.2%) and selectivity alterations were clearly observed in 35 to 50 hours, while final CH_4 selectivity increased to 74.7% and the STY of C_{2+} HCs dropped from 7.6 to 2.6 mmol g^{-1} $hour^{-1}$ within 50 hours on stream (fig. S33). By comparison, with co-feeding 0.5% H_2O (Fig. 6D), the K-Co_2C catalyst showed higher stability throughout a 210-hour test. The final selectivity to C_{2+} HCs remained at 49.2%, exceeding 90% of the initial values (53.0%, at 15 hours), and the STY of C_{2+} HCs still retained 7.2 mmol g^{-1} $hour^{-1}$ at 210 hours. The XRD patterns of spent samples (fig. S34) show that co-feeding 25% H_2O caused the complete decomposition of Co_2C, which is in accordance with the in situ XRD results (Fig. 4E). However, no substantial difference was observed in spent samples with co-feeding 0.5 or 2.5% H_2O, indicating that their evolution mainly occurs on the catalytic surface. The quasi in situ XPS spectra of the spent K-Co_2C with 0.5% H_2O are shown in Fig. 6 (E and F). The binding energies of Co $2p_{1/2}$ and Co$2p_{3/2}$ at 793.5 and 778.3 eV reveal that the catalytic surface is Co_2C. Notably, the addition of 0.5% H_2O enhances the signal of the Co—C bond at 283.1 eV (C 1s spectra) in comparison to the results of the K-Co_2C sample which was used without co-feeding H_2O (Fig. 2F). The estimated surface C/Co ratio increased from 0.27 (without H_2O) to 0.46 with co-feeding 0.5% H_2O, particularly substantiating that the decomposition of Co_2C has been inhibited by adding moderate H_2O in the reaction.

In conclusion, we provide an in situ synthesized and stable K-Co_2C catalyst for CO_2 hydrogenation which shows outstanding activity and selectivity to C_{2+} HCs up to 67.3% at 300°C, 3.0 MPa. Compared with metallic cobalt catalysts, K-Co_2C is more competitive in accelerating the formation of C_{2+} HCs, and a C-rich and H-lean surface environment suppresses the side reaction toward CH_4. This K-Co_2C catalyst is promising to be combined with the zeolites or membrane reactors to further optimize the product composition and alleviate the downstream separation needs for improving its practical applications (3, 59). Adsorbed CO derived from carbonate splitting is an important intermediate for coupling to C_{2+} HCs as confirmed by in situ DRIFTS. Multispectral studies, including in situ XRD, quasi in situ XPS, and DFT calculations, reveal that Co_2C is directly generated from CoO instead of undergoing the reduction to Co^0. The reactants (H_2 and CO_2) or the product (H_2O) of high concentrations all can cause the decomposition of Co_2C to Co^0, while the delicate balance of the reaction atmosphere and the K promoter plays vital roles in the stabilization of Co_2C. Co-feeding a small amount of H_2O instead facilitates the carburization and stabilization of Co_2C. During the carburization, 2% H_2O and the K

promoter jointly act on the CoO surface and stimulate the formation of key $CO_2^{\delta-}$ species, followed by its dissociation to active C^* species. The K promoter also enables the subsequent C^* adsorption on the CoO surface, favoring the C accumulation and permeation. Inspired by this finding, 0.5% H_2O was co-fed in the feed gas to stabilize the surface structure of K-Co_2C and it markedly prolongs the catalytic stability from 35 to over 200 hours. Given that H_2O is an inevitable impurity in the flue gas (a key source for CO_2 capture) and generally considered a poison in CO_2 hydrogenation reaction, our study highlights the unique promoting effect of H_2O in feed gas on Co_2C catalyst and it is expected to improve its practical application in CO_2 conversion. However, considering that the excessive H_2O addition is conversely detrimental to Co_2C, its separation before the catalytic conversion or the surface hydrophobic or hydrophilic modifications to control its content within the ideal range is still needed. The fundamental understanding of the formation and stabilization of Co_2C also provides opportunities for its potential application in other reactions.

MATERIALS AND METHODS
Catalyst preparation
Synthesis of Co_3O_4 and modified Co_3O_4 precursor
$Co(NO_3)_2·6H_2O$ was purchased from Aladdin Biochemical Technology Co., Ltd. Citric acid, Na_2CO_3, K_2CO_3, and Cs_2CO_3 were purchased from Bodi Chemical Trade Co., Ltd. Co_3O_4 precursor was prepared using a citric acid–induced sol-gel method. Typically, citric acid and $Co(NO_3)_2·6H_2O$ (molar ratio = 13/20) were dissolved in ethanol and the mixed solution was aged at 30°C for hydrolysis and complexation. Then, the ethanol was fully evaporated at 80°C. The obtained foamy gel was dried at 80°C for 12 hours and further calcined in air at 450°C for 4 hours to get the Co_3O_4 precursor.

Alkali metal–modified Co_3O_4 precursors were synthesized by an IWI method using an aqueous solution of their carbonates. The molar amount of Na_2CO_3 or Cs_2CO_3 was fixed as 0.025 mmol, whereas that of K_2CO_3 was tried as 0.013, 0.025, and 0.050 mmol (the corresponding mass fractions of K are 0.49, 0.98, and 1.96%). As an example, 0.0035 g (0.025 mmol) of K_2CO_3 was dissolved in 0.12 g of H_2O through sonication, and then the solution was dropped on 0.2 g of Co_3O_4 under stirring at room temperature. The resulting power was dried at 80°C for 12 hours and calcined in air at 400°C for 2 hours to get the 0.98% K-Co_3O_4 precursor.

Synthesis of testing samples
We used the in situ XRD reactor chamber to prepare the samples which were denoted as K-CoO, K-Co^0, CoO-t, and Co_2C-t, respectively. The K-CoO sample was prepared from the reduction of 0.98% K-Co_3O_4 in H_2 at 240°C, 0.8 MPa. The K-Co^0 sample was obtained from the decomposition of K-Co_2C in H_2 at 340°C, 0.8 MPa. The CoO-t sample was prepared from the reduction of Co_3O_4 precursor in H_2 at 220°C, 0.1 MPa. The Co_2C-t sample was prepared from two-step treatments from Co_3O_4 precursor, including the initial reduction at 260°C, and the following carburization in CO, as recorded in fig. S23A. Before the ex situ structural characterizations, the Co^0-t and K-Co_2C samples were carefully passivated in the flow of 1% O_2/N_2 (20 ml min^{-1}) at ~20°C for 1 hour and then were transferred to the glove box for preservation.

Catalyst characterization

XRD patterns were recorded on a Rigaku SmartLab 9-kW diffractometer with Cu Kα radiation (λ = 1.5406 Å) and with a scanning rate of 8°/min. In situ XRD measurements were performed in an XRK 900 reactor chamber and the heating process was controlled by a TCU 750 temperature control unit. The patterns were collected for each 10 min until the structure is stable for at least 1 hour at the given conditions. As for the structural evolution in CO_2 hydrogenation, the sample was directly heated to the target temperature in the reactive gas at 0.8 MPa. For the structural evolution in other atmospheres ($H_2/CO_2/CO/H_2O$), the specific conditions were introduced in the corresponding results.

Quasi in situ XPS was performed on a spectrometer equipped with an Al K x-ray source at 300 W. Before the test, the samples, including the K-Co$_2$C and Co^0-t (without the passivation), were carefully transferred from the glove box to the XPS analysis chamber without the exposure to air. Besides, the carburization processes for CoO-t and K-CoO samples were simulated in 10% CO/N$_2$ or 10% CO + 2% H$_2$O/N$_2$ in the reaction chamber equipped with the NAP-XPS system. Here, these quasi in situ XPS spectra were recorded after reaching the setting temperatures for 20 min. The thermal couples were placed at the side of the powder sample for in situ XRD (set temperature, ±30°C) and on the upper surface of the sample piece for quasi in stu XPS, respectively (fig. S35).

In situ DRIFTS experiments were performed using the Thermo Scientific Nicolet iS50 spectrometer with a mercury cadmium telluride detector, and the background spectrum was collected after N$_2$ purge for at least 1 hour. The flow rate of reactive gas (CO$_2$/H$_2$/N$_2$ = 21:63:16) or N$_2$ is 30 ml min^{-1}, whereas that of CO$_2$, CO, or H$_2$ is 10 ml min^{-1}. As for mechanism studies on K-Co$_2$C and Co^0-t samples, the testing temperature is not above 260°C for avoiding the destroy from CO$_2$ or H$_2$ on catalyst structure. As shown in fig. S36, these samples were in situ synthesized in the IR cell at 300°C, 1.2 MPa for 3 hours, and then was purged (300°C) and cooled (50°C) in N$_2$, atmospheric pressure before the adsorption of CO$_2$ and the following switching to H$_2$. The co-fed H$_2$O at atmospheric pressure for in situ XRD or DRIFTS and quasi in situ XPS test is stored in a glass wash bottle, which is placed before the reactor chamber. Its content is dependent on the controlled temperature of wash bottle. The theoretical H$_2$O content was calculated according to the following equation and was used for the expression. The actual H$_2$O content was determined using the NaOH and silica gel as the absorbents (fig. S37), while the above results are listed in table S8.

$$\text{Theoretical Content}_{H_2O} = \frac{p^*_{H_2O}}{p_0} \times 100\%$$

TPD tests were carried out on a Quantachrome ChemBET Pulsar analyzer, while the desorbed species was detected by the Pfeiffer GSD-350 online MS. Typically, the samples were loaded into a quartz tube and flushed with N$_2$ at 300°C for 1 hour to remove undesired adsorbates, and then cooled to room temperature. The samples were first retreated in the reactive gas at 300°C for 1 hour to remove the external passivation layer, and then flushed with N$_2$ for 1 hour. These samples were cooled to 30°C to adsorb CO$_2$ or CO in 1 hour, followed by switching to N$_2$ to purge for 30 min. Then, the desorption and analysis program were conducted with a heating rate of 10°C min^{-1} to 700°C.

TEM and HRTEM images were obtained on a Tecnai F30 HRTEM instrument (FEI Corp) with a voltage of 300 kV. EDS elemental mapping images were obtained on a JEM ARM200F thermal-field emission microscope equipped with a probe spherical aberration (Cs) corrector with a voltage of 200 kV. UV Raman spectra were collected on a homemade triple-stage UV Raman spectrometer with a resolution of 2 cm^{-1}. The wavelength of UV laser line from a double-frequency 514-nm laser was set at 320 nm. The textural properties were determined by Ar absorption-desorption on a Quantachrome AUTO-SORB-1-MP sorption at 87 K. The surface area was calculated using the Brunauer-Emmett-Teller (BET) method. The concentrations of alkali metals and Co were determined by inductively coupled plasma optical emission spectrometry on a PerkinElmer AVIO 500 instrument and the results are listed in table S9. TGA was conducted on a TGA-SDTA851e thermobalance in the air flow (25 ml min^{-1}) with a heating rate of 5°C min^{-1} from 50° to 800°C.

Catalytic activity test

The CO$_2$ hydrogenation was conducted in a stainless steel fixed-bed flow reactor with an 8-mm inner diameter. A total of 150 mg of Co$_3$O$_4$ or alkali metal–modified Co$_3$O$_4$ precursor (20 to 40 meshes) was diluted with 450 mg of quartz sand (20 to 40 meshes), and then loaded into the middle of the reactor. Catalytic performance was tested in the reactive gas (CO$_2$/H$_2$/Ar = 1:3:1.5, space velocity = 6000 ml g^{-1} hour^{-1}, P = 3.0 MPa unless otherwise noted) at 260°, 300°, and 340°C. The products were collected at about 3 hours after reaching the steady state on steam. As shown in fig. S38, all the products, including the liquid oxygenates and C$_{5+}$ HCs, were heated by an oven and heating belt at 100°C for full vaporization and accessed into the online chromatography (Agilent, 7890B) for the analysis by the thermal conductivity detector and flame ionization detector, while the Ar was used as an internal standard. CO$_2$ conversion and CO selectivity were calculated on a carbon-atom basis according to the following equations

$$CO_2 \ \text{Conv.}(\%) = \frac{n_{CO_2,in} - n_{CO_2,out}}{n_{CO_2,in}} \times 100\%$$

$$CO \ \text{Sel.}(\%) = \frac{n_{CO,out}}{n_{CO_2,in} - n_{CO_2,out}} \times 100\%$$

where $n_{CO_2,in}$ and $n_{CO_2,out}$ represent the concertation of CO$_2$ at the inlet and outlet. $n_{CO,out}$ represents the CO concertation at the outlet. The total selectivity of alcohols and dimethyl ether is below 1.5% and therefore was not reported here.

The selectivity to HC C$_n$H$_m$ was calculated for representing the HCs distribution

$$C_nH_m \ \text{Sel.}(\%) = \frac{nC_nH_{m,out}}{\Sigma \ iC_iH_{m,out}} \times 100\%$$

where C$_n$H$_{m,out}$ represents moles of detected individual HCs product.

The STY, the O/P ratio, and the chain growth factor α were calculated as shown below

$$\text{STY}^a \,(\text{mmol}\,\text{g}^{-1}\,\text{h}^{-1}) = \frac{\text{CO}_2\,\text{Conv.} \times \text{C}_n\text{H}_m\,\text{Sel.} \times (1 - \text{CO Sel.}) \times 6000}{22.4 \times 5.5}$$

$$\text{STY}^b \,(\text{mmol}\,\text{m}^{-2}\,\text{h}^{-1}) = \frac{\text{STY}^a}{S_{\text{BET}}}$$

$$\text{O/P ratio} = \frac{\text{Sel.}(C_2 \sim C_4^=)}{\text{Sel.}(C_2 \sim C_4^0)}$$

$$\ln\frac{W_n}{n} = n \cdot \ln\alpha + n\frac{(1-\alpha)^2}{\alpha}$$

where STY^a and STY^b represent the STY values normalized based on catalyst mass and surface area (S_{BET}; table S4). W_n and n represent the mass fraction and the carbon number of HCs products. The carbon balance was in the range of 95 to 105%.

The contents (0.25 to 25%) of H_2O mentioned in this work represent those of extra-added H_2O in the carburization gas or feed gas. The H_2O was added using a steel gas wash bottle, which can be pressurized to 3.0 MPa, and the setting temperatures are listed in table S8. For the kinetics tests (activation energy and reaction order), the conversion was decreased below 10% by varying the space velocity.

Theory computational methods
The basic thermodynamic calculations (ΔG, ΔH, and ΔS) were carried out by the Aspen Plus V11 software. All spin-polarized DFT calculations were performed with the Vienna Ab initio Simulation Package. The exchange-correlation energies were calculated by the generalized gradient approximation approach with the Perdew-Burke-Ernzerhof functional (60). Core electrons were frozen and treated with the projector-augmented wave theory (61). Valence electrons were taken as Co ($4s^2 3d^7$), C ($2s^2 2p^2$), and O ($2s^2 2p^4$). The plane-wave basis set was truncated at 500 eV for gas molecules and surface calculations and was increased to 650 eV for bulk crystals to mitigate the effect from Pulay stress. Gaussian smearing with 0.1-eV width was applied to oxides and molecules while first order of Methfessel-Paxton smearing was applied to metal and carbides (62). Brillouin zones were treated with the Monkhorst-Pack k-points mesh (63). The k-points, lattice parameters, space groups, and magnetics are summarized in table S10. The van der Waals interaction correction was applied for all calculations with the DFT-D3 method (64). The climbing image nudged elastic band method was used to find transition states, combined with the dimer method. It was verified that each transition state had only one imaginary vibrational frequency along the reaction coordinate direction. A three-layer slab model was built for the CoO (200) surface and the bottom two layers were fixed during structural optimization. The criteria of force convergence for surface calculations were set to 0.03 eV/Å on all atoms. The Hubbard U-correction was applied to oxides for localized d-state electrons (65). A value of 3.3 eV for Co was taken from the work of Wang et al. (66). Bader charge analysis was performed to investigate the charge transfer of the adsorbate-surface system (67). The adsorption and activation of CO_2 and H_2 were investigated on Co_2C (101) and (020) surfaces, and the

Co (002) surface. All surface calculations were performed in the Monkhorst-Pack scheme using k-points of $2 \times 2 \times 1$ with the addition of a vacuum layer of 15 Å to avoid interactions between repeating periodic elements. In the structural optimization of Co_2C surfaces, the bottom 1/3 Co and C atoms are fixed in their original atomic positions, while the remaining top 2/3 Co and C atoms together with the adsorbate are completely relaxed. We constructed three kinds of CoO (200) surfaces: clean surface, surface containing only K_2O, and surface containing both K_2O and H_2O, and calculated the reaction energy of the stepwise decomposition of $CO_2^{\delta-}$ to C^* species on these three surfaces. The optimized structures involved are displayed in figs. S39 and S40, respectively.

Ab initio thermodynamics (68) was applied to construct the bulk phase diagram, locate the reaction conditions on the resulting phase diagram, and calculate formation energies. The explanation pertaining to the equilibrium assumptions inherent to this thermodynamics method is shown in the Supplementary Materials. In the bulk phase diagram, the phase with lowest formation energy is identified as the stable phase. The chemical potentials of C and O are determined by the free energies of the gas species with the assumption that the gas phase is equilibrated with the catalysts. The free energy of a molecule is calculated according to the following equations

$$\mu_O = G_{CO_2} - G_{CO}$$

$$\mu_C = G_{CO} - \mu_O$$

$$G_{\text{gas}} = E_{\text{gas}}^{\text{DFT}} + \text{ZPE}_{\text{gas}} + \Delta H_{\text{gas}}^{0K \to 533.15K} - TS_{\text{gas}}^{533.15K} + RT \cdot \ln\frac{p_{\text{gas}}}{p_{\text{ref}}}$$

where G_{CO_2} and G_{CO} are the free energy of CO_2 and CO. G_{gas} is the free energy of the gas molecule, $E_{\text{gas}}^{\text{DFT}}$ is the DFT energy of the gas molecule, ZPE_{gas} is the zero-point vibrational energy of the gas molecule, $\Delta H_{\text{gas}}^{0K \to 533.15K}$ is the enthalpy change of the gas molecule from 0 to 533.15 K, T is set as 533.15 K according to the initial carburization temperature for K-Co_3O_4 sample, and $S_{\text{gas}}^{533.15K}$ is the entropy of the gas molecule at 533.15 K, R is the gas constant, p_{gas} is the partial pressure of the gas, and p_{ref} is the reference pressure, which is set to 1 bar. The following temperature and partial pressures were used in determining the chemical potential of O and C in Fig. 4B: red dot (533.15 K, 1.45 bar CO_2, 1×10^{-10} bar CO), black dot (533.15 K, 1.45 bar CO_2, 1.645×10^{-3} CO). The pressure of CO was set to 1×10^{-10} bar to represent that it does not exist in the initial reaction condition, while all other partial pressures were measured from our experiments.

The average formation energy ΔE_{form} of each C atom adsorption on the CoO (200) surface with or without the co-adsorption of K_2O is defined with the following equation

$$\Delta E_{\text{form}} = (E_{\text{total}} - E_{\text{sur}} - z \cdot \mu_C^0)/z$$

where E_{total} is the total DFT energy of a surface adsorption structure with z C atoms, E_{sur} is the DFT energy of the clean CoO surface (either with or without co-adsorbed K_2O). z is set as 2 and 3, while μ_C^0 is set as -8.16 eV on the basis of the above calculation result of the chemical potential of carbon.

Supplementary Materials

This PDF file includes:
Supplementary Text
Figs. S1 to S40
Tables S1 to S10

REFERENCES AND NOTES

1. P. Falkowski, R. J. Scholes, E. Boyle, J. Canadell, D. Canfield, J. Elser, N. Gruber, K. Hibbard, P. Högberg, S. Linder, F. T. Mackenzie, B. Moore III, T. Pedersen, Y. Rosenthal, S. Seitzinger, V. Smetacek, W. Steffen, The global carbon cycle: A test of our knowledge of earth as a system. *Science* **290**, 291–296 (2000).

2. B. Zhao, M. Sun, F. Chen, Y. Shi, Y. Yu, X. Li, B. Zhang, Unveiling the activity origin of iron nitride as catalytic material for efficient hydrogenation of CO_2 to C_{2+} hydrocarbons. *Angew. Chem. Int. Ed. Engl.* **60**, 4496–4500 (2021).

3. J. Wei, R. Yao, Y. Han, Q. Ge, J. Sun, Towards the development of the emerging process of CO_2 heterogenous hydrogenation into high-value unsaturated heavy hydrocarbons. *Chem. Soc. Rev.* **50**, 10764–10805 (2021).

4. L. Fan, C. Xia, F. Yang, J. Wang, H. Wang, Y. Lu, Strategies in catalysts and electrolyzer design for electrochemical CO_2 reduction toward C_{2+} products. *Sci. Adv.* **6**, eaay3111 (2020).

5. R. P. Ye, J. Ding, W. Gong, M. D. Argyle, Q. Zhong, Y. Wang, C. K. Russell, Z. Xu, A. G. Russell, Q. Li, M. Fan, Y. G. Yao, CO_2 hydrogenation to high-value products via heterogeneous catalysis. *Nat. Commun.* **10**, 5698 (2019).

6. W. Zhou, K. Cheng, J. Kang, C. Zhou, V. Subramanian, Q. Zhang, Y. Wang, New horizon in C1 chemistry: Breaking the selectivity limitation in transformation of syngas and hydrogenation of CO_2 into hydrocarbon chemicals and fuels. *Chem. Soc. Rev.* **48**, 3193–3228 (2019).

7. H. M. T. Galvis, J. H. Bitter, C. B. Khare, M. Ruitenbeek, A. I. Dugulan, K. P. de Jong, Supported iron nanoparticles as catalysts for sustainable production of lower olefins. *Science* **335**, 835–838 (2012).

8. Y. Xu, X. Li, J. Gao, J. Wang, G. Ma, X. Wen, Y. Yang, Y. Li, M. Ding, A hydrophobic FeMn@Si catalyst increases olefins from syngas by suppressing C1 by-products. *Science* **371**, 610–613 (2021).

9. Y. Han, C. Fang, X. Ji, J. Wei, Q. Ge, J. Sun, Interfacing with carbonaceous potassium promoters boosts catalytic CO_2 hydrogenation of iron. *ACS Catal.* **10**, 12098–12108 (2020).

10. T. Lin, F. Yu, Y. An, T. Qin, L. Li, K. Gong, L. Zhong, Y. Sun, Cobalt carbide nanocatalysts for efficient syngas conversion to value-added chemicals with high selectivity. *Acc. Chem. Res.* **54**, 1961–1971 (2021).

11. L. Zhong, F. Yu, Y. An, Y. Zhao, Y. Sun, Z. Li, T. Lin, Y. Lin, X. Qi, Y. Dai, L. Gu, J. Hu, S. Jin, Q. Shen, H. Wang, Cobalt carbide nanoprisms for direct production of lower olefins from syngas. *Nature* **538**, 84–87 (2016).

12. Z. Li, L. Zhong, F. Yu, Y. An, Y. Dai, Y. Yang, T. Lin, S. Li, H. Wang, P. Gao, Y. Sun, M. He, Effects of sodium on the catalytic performance of comn catalysts for Fischer-Tropsch to olefin reactions. *ACS Catal.* **7**, 3622–3631 (2017).

13. C. Zhang, S. Li, L. Zhong, Y. Sun, Theoretical insights into morphologies of alkali-promoted cobalt carbide catalysts for Fischer-Tropsch synthesis. *J. Phy. Chem. C* **125**, 6061–6072 (2021).

14. Z. Li, T. Lin, F. Yu, Y. An, Y. Dai, S. Li, L. Zhong, H. Wang, P. Gao, Y. Sun, M. He, Mechanism of the Mn promoter via CoMn spinel for morphology control: Formation of Co_2C nanoprisms for Fischer-Tropsch to olefins reaction. *ACS Catal.* **7**, 8023–8032 (2017).

15. Z. Li, D. Yu, L. Yang, J. Cen, K. Xiao, N. Yao, X. Li, Formation mechanism of the Co_2C nanoprisms studied with the CoCe system in the Fischer-Tropsch to olefin reaction. *ACS Catal.* **11**, 2746–2753 (2021).

16. R. Yang, Z. Xia, Z. Zhao, F. Sun, X. Du, H. Yu, S. Gu, L. Zhong, J. Zhao, Y. Ding, Z. Jiang, Characterization of CoMn catalyst by in situ x-ray absorption spectroscopy and wavelet analysis for Fischer-Tropsch to olefins reaction. *J. Energy Chem.* **32**, 118–123 (2019).

17. J. G. Moya-Cancino, A.-P. Honkanen, A. M. J. van der Eerden, R. Oord, M. Monai, I. ten Have, C. J. Sahle, F. Meirer, B. M. Weckhuysen, F. M. F. de Groot, S. Huotari, In situ x-ray raman scattering spectroscopy of the formation of cobalt carbides in a Co/TiO2 Fischer-Tropsch synthesis catalyst. *ACS Catal.* **11**, 809–819 (2021).

18. T. Lin, K. Gong, C. Wang, Y. An, X. Wang, X. Qi, S. Li, Y. Lu, L. Zhong, Y. Sun, Fischer-Tropsch synthesis to olefins: Catalytic performance and structure evolution of Co_2C-based catalysts under a CO_2 environment. *ACS Catal.* **9**, 9554–9567 (2019).

19. T. Fan, H. Liu, S. Shao, Y. Gong, G. Li, Z. Tang, Cobalt catalysts enable selective hydrogenation of CO_2 toward diverse products: Recent progress and perspective. *J. Phys. Chem. Lett.* **12**, 10486–10496 (2021).

20. M. K. Gnanamani, G. Jacobs, R. A. Keogh, W. D. Shafer, D. E. Sparks, S. D. Hopps, G. A. Thomas, B. H. Davis, Fischer-Tropsch synthesis: Effect of pretreatment conditions of cobalt on activity and selectivity for hydrogenation of carbon dioxide. *Appl. Catal. A* **499**, 39–46 (2015).

21. S. Zhang, X. Liu, Z. Shao, H. Wang, Y. Sun, Direct CO_2 hydrogenation to ethanol over supported Co_2C catalysts: Studies on support effects and mechanism. *J. Catal.* **382**, 86–96 (2020).

22. S. Zhang, X. Liu, H. Luo, Z. Wu, B. Wei, Z. Shao, C. Huang, K. Hua, L. Xia, J. Li, L. Liu, W. Ding, H. Wang, Y. Sun, Morphological modulation of Co_2C by surface-adsorbed species for highly effective low-temperature CO_2 reduction. *ACS Catal.* **12**, 8544–8557 (2022).

23. Z. Shi, Y. Tao, J. Wu, C. Zhang, H. He, L. Long, Y. Lee, T. Li, Y. B. Zhang, Robust metal-triazolate frameworks for CO_2 capture from flue gas. *J. Am. Chem. Soc.* **142**, 2750–2754 (2020).

24. J. Zhu, P. Wang, X. Zhang, G. Zhang, R. Li, W. Li, T. P. Senftle, W. Liu, J. Wang, Y. Wang, A. Zhang, Q. Fu, C. Song, X. Guo, Dynamic structural evolution of iron catalysts involving competitive oxidation and carburization during CO_2 hydrogenation. *Sci. Adv.* **8**, eabm3629 (2022).

25. G. L. Bezemer, T. J. Remans, A. P. v. Bavel, A. I. Dugulan, Direct evidence of water-assisted sintering of cobalt on carbon nanofiber catalysts during simulated Fischer-Tropsch conditions revealed with in situ Mössbauer spectroscopy. *J. Am. Chem. Soc.* **132**, 8540–8541 (2010).

26. N. E. Tsakoumis, J. C. Walmsley, M. Ronning, W. van Beek, E. Rytter, A. Holmen, Evaluation of reoxidation thresholds for γ-Al_2O_3-supported cobalt catalysts under Fischer-Tropsch synthesis conditions. *J. Am. Chem. Soc.* **139**, 3706–3715 (2017).

27. M. Wolf, E. K. Gibson, E. J. Olivier, J. H. Neethling, C. R. A. Catlow, N. Fischer, M. Claeys, Water-induced formation of cobalt-support compounds under simulated high conversion Fischer-Tropsch environment. *ACS Catal.* **9**, 4902–4918 (2019).

28. W. Fang, C. Wang, Z. Liu, L. Wang, L. Liu, H. Li, S. Xu, A. Zheng, X. Qin, L. Liu, F.-S. Xiao, Physical mixing of a catalyst and a hydrophobic polymer promotes CO hydrogenation through dehydration. *Science* **377**, 406–410 (2022).

29. Y. An, T. Lin, F. Yu, X. Wang, Y. Lu, L. Zhong, H. Wang, Y. Sun, Effect of reaction pressures on structure–performance of Co_2C-based catalyst for syngas conversion. *Ind. Eng. Chem. Res.* **57**, 15647–15653 (2018).

30. M. Xu, C. Cao, J. Xu, Understanding kinetically interplaying reverse water-gas shift and Fischer-Tropsch synthesis during CO_2 hydrogenation over Fe-based catalysts. *Appl. Catal. A* **641**, 118682 (2022).

31. Z. Zhao, W. Lu, R. Yang, H. Zhu, W. Dong, F. Sun, Z. Jiang, Y. Lyu, T. Liu, H. Du, Y. Ding, Insight into the formation of Co@Co_2C catalysts for direct synthesis of higher alcohols and olefins from syngas. *ACS Catal.* **8**, 228–241 (2018).

32. R. Zhang, G. Wen, H. Adidharma, A. G. Russell, B. Wang, M. Radosz, M. Fan, C_2 oxygenate synthesis via Fischer-Tropsch synthesis on Co_2C and Co/Co_2C interface catalysts: How to control the catalyst crystal facet for optimal selectivity. *ACS Catal.* **7**, 8285–8295 (2017).

33. J. Wang, G. Li, Z. Li, C. Tang, Z. Feng, H. An, H. Liu, T. Liu, C. Li, A highly selective and stable ZnO-ZrO_2 solid solution catalyst for CO_2 hydrogenation to methanol. *Sci. Adv.* **3**, e1701290 (2017).

34. P. P. Paalanen, S. H. van Vreeswijk, B. M. Weckhuysen, Combined in situ x-ray powder diffractometry/raman spectroscopy of iron carbide and carbon species evolution in Fe(−Na−S)/α-Al_2O_3 catalysts during Fischer-Tropsch synthesis. *ACS Catal.* **10**, 9837–9855 (2020).

35. S. Selvakumar, N. Nuns, M. Trentesaux, V. S. Batra, J. M. Giraudon, J. F. Lamonier, Reaction of formaldehyde over birnessite catalyst: A combined XPS and ToF-SIMS study. *Appl Catal B* **223**, 192–200 (2018).

36. T. Lin, P. Liu, K. Gong, Y. An, F. Yu, X. Wang, L. Zhong, Y. Sun, Designing silica-coated CoMn-based catalyst for Fischer-Tropsch synthesis to olefins with low CO_2 emission. *Appl Catal B* **299**, 120683 (2021).

37. Y. Jiang, R. Long, Y. Xiong, Regulating C-C coupling in thermocatalytic and electrocatalytic CO_x conversion based on surface science. *Chem. Sci.* **10**, 7310–7326 (2019).

38. H. Jo, M. K. Khan, M. Irshad, M. W. Arshad, S. K. Kim, J. Kim, Unraveling the role of cobalt in the direct conversion of CO_2 to high-yield liquid fuels and lube base oil. *Appl Catal B* **305**, 121041 (2022).

39. X. Wang, X. Zeng, N. Gong, T. Zhang, Y. Wu, J. Zhang, F. Song, G. Yang, Y. Tan, Effective suppression of CO selectivity for CO_2 hydrogenation to high-quality gasoline. *ACS Catal.* **11**, 1528–1547 (2021).

40. M. Lei, B. Hong, L. Yan, R. Chen, F. Huang, Y. Zheng, Enhanced stability for preferential oxidation of CO in H_2 under H_2O and CO_2 atmosphere through interaction between iridium and copper species. *Int. J. Hydrogen Energy* **47**, 24374–24387 (2022).

41. L. Lukashuk, N. Yigit, R. Rameshan, E. Kolar, D. Teschner, M. Havecker, A. Knop-Gericke, R. Schlogl, K. Fottinger, G. Rupprechter, Operando insights into CO oxidation on cobalt oxide catalysts by NAP-XPS, FTIR, and XRD. *ACS Catal.* **8**, 8630–8641 (2018).

42. J. Zhu, Y. Su, J. Chai, V. Muravev, N. Kosinov, E. J. Hensen, Mechanism and nature of active sites for methanol synthesis from CO/CO_2 on Cu/CeO_2. *ACS Catal.* **10**, 11532–11544 (2020).

43. Y. Lv, P. Wang, D. Liu, F. Zhang, T. P. Senftle, G. Zhang, Z. Zhang, J. Huang, W. Liu, Tracing the active phase and dynamics for carbon nanofiber growth on nickel catalyst using environmental transmission electron microscopy. *Small methods* **6**, 2200235 (2022).

44. E. de Smit, B. M. Weckhuysen, The renaissance of iron-based Fischer-Tropsch synthesis: On the multifaceted catalyst deactivation behaviour. *Chem. Soc. Rev.* **37**, 2758–2781 (2008).

45. E. de Smit, F. Cinquini, A. M. Beale, O. V. Safonova, W. van Beek, P. Sautet, B. M. Weckhuysen, Stability and reactivity of ε-χ-θ iron carbide catalyst phases in Fischer-Tropsch synthesis: Controlling μC. *J. Am. Chem. Soc.* **132**, 14928–14941 (2010).

46. M. Wolf, N. Fischer, M. Claeys, Formation of metal-support compounds in cobalt-based Fischer-Tropsch synthesis: A review. *Chem Catal.* **1**, 1014–1041 (2021).

47. W. Li, X. Nie, H. Yang, X. Wang, F. Polo-Garzon, Z. Wu, J. Zhu, J. Wang, Y. Liu, C. Shi, C. Song, X. Guo, Crystallographic dependence of CO_2 hydrogenation pathways over HCP-Co and FCC-Co catalysts. *Appl Catal B* **315**, 121529 (2022).

48. L. M. van Koppen, A. Iulian Dugulan, G. Leendert Bezemer, E. J. M. Hensen, Sintering and carbidization under simulated high conversion on a cobalt-based Fischer-Tropsch catalyst; manganese oxide as a structural promotor. *J. Catal.* **413**, 106–118 (2022).

49. M. Wolf, B. K. Mutuma, N. J. Coville, N. Fischer, M. Claeys, Role of CO in the water-induced formation of cobalt oxide in a high conversion Fischer-Tropsch environment. *ACS Catal.* **8**, 3985–3989 (2018).

50. M. Claeys, M. E. Dry, E. van Steen, P. J. van Berge, S. Booyens, R. Crous, P. van Helden, J. Labuschagne, D. J. Moodley, A. M. Saib, Impact of process conditions on the sintering behavior of an alumina-supported cobalt Fischer-Tropsch catalyst studied with an in situ magnetometer. *ACS Catal.* **5**, 841–852 (2015).

51. L. Nguyen, F. F. Tao, Y. Tang, J. Dou, X. J. Bao, Understanding catalyst surfaces during catalysis through near ambient pressure x-ray photoelectron spectroscopy. *Chem. Rev.* **119**, 6822–6905 (2019).

52. L. Chen, S. Ren, X. Xing, J. Yang, X. Li, M. Wang, Z. Chen, Q. Liu, Poisoning mechanism of KCl, K_2O and SO_2 on Mn-Ce/CuX catalyst for low-temperature SCR of NO with NH_3. *Process Saf. Environ. Prot.* **167**, 609–619 (2022).

53. F. Romero-Sarria, L. F. Bobadilla, E. M. Jiménez Barrera, J. A. Odriozola, Experimental evidence of HCO species as intermediate in the fischer tropsch reaction using operando techniques. *Appl Catal B* **272**, 119032 (2020).

54. L. F. Bobadilla, J. L. Santos, S. Ivanova, J. A. Odriozola, A. Urakawa, Unravelling the role of oxygen vacancies in the mechanism of the reverse water–gas-shift reaction by *operando* DRIFTS and UV–Vis spectroscopy. *ACS Catal.* **8**, 7455–7467 (2018).

55. R. Liu, D. Leshchev, E. Stavitski, M. Juneau, J. N. Agwara, M. D. Porosoff, Selective hydrogenation of CO_2 and CO over potassium promoted Co/ZSM-5. *Appl Catal B* **284**, 119787 (2021).

56. P. Gonugunta, A. I. Dugulan, G. L. Bezemer, E. Brück, Role of surface carboxylate deposition on the deactivation of cobalt on titania Fischer-Tropsch catalysts. *Catal. Today* **369**, 144–149 (2021).

57. L. Falbo, C. G. Visconti, L. Lietti, J. Szanyi, The effect of CO on CO_2 methanation over Ru/Al_2O_3 catalysts: A combined steady-state reactivity and transient DRIFT spectroscopy study. *Appl Catal B* **256**, 117791 (2019).

58. E. Rytter, A. Holmen, Perspectives on the effect of water in cobalt Fischer-Tropsch synthesis. *ACS Catal.* **7**, 5321–5328 (2017).

59. H. Li, C. Qiu, S. Ren, Q. Dong, S. Zhang, F. Zhou, X. Liang, J. Wang, S. Li, M. Yu, Na^+-gated water-conducting nanochannels for boosting CO_2 conversion to liquid fuels. *Science* **367**, 667–671 (2020).

60. G. Kresse, J. Furthmiiller, Efficiency of ab-initio total energy calculations for metals and semiconductors using a plane-wave basis set. *Comput. Mater. Sci.* **6**, 15–50 (1996).

61. P. E. Blochl, Projector augmented-wave method. *Phys. Rev. B* **50**, 17953–17979 (1994).

62. M. Methfessel, A. T. Paxton, High-precision sampling for Brillouin-zone integration in metals. *Phys. Rev. B* **40**, 3616–3621 (1989).

63. H. J. Monkhorst, J. D. Pack, Special points for Brillouin-zone integrations. *Phys. Rev. B* **13**, 5188–5192 (1976).

64. S. Grimme, J. Antony, S. Ehrlich, H. Krieg, A consistent and accurate ab initio parametrization of density functional dispersion correction (DFT-D) for the 94 elements H-Pu. *J. Chem. Phys.* **132**, 154104 (2010).

65. S. L. Dudarev, G. A. Botton, S. Y. Savrasov, C. J. Humphreys, A. P. Sutton, Electron-energy-loss spectra and the structural stability of nickel oxide: An LSDA+U study. *Phys. Rev. B* **57**, 1505–1509 (1998).

66. L. Wang, T. Maxisch, G. Ceder, Oxidation energies of transition metal oxides within the GGA+U framework. *Phys. Rev. B* **73**, 195107 (2006).

67. G. Henkelman, A. Arnaldsson, H. Jónsson, A fast and robust algorithm for Bader decomposition of charge density. *Comput. Mater. Sci.* **36**, 354–360 (2006).

68. S. Blomberg, H. Bluhm, J. A. v. Bokhoven, M. Bracconi, A. Cuoci, J. Frenken, I. Groot, J. Gustafson, U. Hartfelder, O. Karslıoğlu, P. J. Kooyman, E. Lundgren, M. Maestri, M. Nachtegaal, S. Rebughini, K. Reuter, A. Stierle, Z. Zetterberg, J. Zhou, *Operando Research in Heterogeneous Catalysis*. A. W. Castleman, J. P. Toennies, K. Yamanouchi, W. Zinth, Eds., (Springer International Publishing, 2017), vol. 114.

Science Advances

Stabilizing Co$_2$C with H$_2$O and K promoter for CO$_2$ hydrogenation to C$_{2+}$ hydrocarbons

Mingrui Wang, Peng Wang, Guanghui Zhang, Zening Cheng, Mengmeng Zhang, Yulong Liu, Rongtan Li, Jie Zhu, Jianyang Wang, Kai Bian, Yi Liu, Fanshu Ding, Thomas P. Senftle, Xiaowa Nie, Qiang Fu, Chunshan Song, and Xinwen Guo

View the article online
https://www.science.org/doi/10.1126/sciadv.adg0167
Permissions
https://www.science.org/help/reprints-and-permissions

Use of this article is subject to the Terms of service